Stellar population synthesis: the effect of improved Asymptotic Giant Branch models and of interstellar dust on mass-to-light–color relations

Pro Gradu -tutkielma
Turun yliopisto
Fysiikan ja tähtitieteen laitos
Tähtitiede
2010
Tom Into
Tarkastajat:
PhD Laura Portinari
Prof Mauri Valtonen

Contents

0 Introduction

Theoretical evolutionary population synthesis (EPS) is an important tool in the pursuit of understanding the chemo-photometric evolution of galaxies. The photometric properties of an ensemble of stars can be obtained by integrating the light of individual stars making use of current stellar evolutionary models. The most basic form of an EPS model is a simple stellar population (SSP), a population of coeval and chemically homogeneous stars. The robustness and reliability of SSP models is inherited from detailed theoretical stellar tracks and derived isochrones that are tested and verified against observations. SSP models can also be directly tested against observations on their real world counterparts, stellar clusters. The calibrated SSPs can then be used as building blocks for constructing more complex populations. SSPs and derived extended EPS models are a commonplace in the literature. The pioneering work by Tinsley (1980) has been followed by many others, for example Arimoto and Yoshii (1986), Maraston (1998), Bruzual and Charlot (2003) and Bruzual (2007), just to quote a few.

There are two main approaches to computing the luminosities of an SSP. The first one is based on the fuel consumption theorem by Renzini and Buzzoni (1986) which states that *the contribution of stars in any given Post-MS stage to the integrated bolometric luminosity of a SSP is directly proportional to the amount of fuel burned during that stage.* The amount of nuclear fuel burned in each evolutionary stage is derived from the stellar evolutionary models and converted into bolometric luminosities according to the fuel consumption theorem and further into luminosities in specific passbands via color transformations. The second approach is the isochrone synthesis method in which the luminosities are obtained by integrating the flux contributions of all mass bins along one isochrone, after assuming an initial mass function (IMF). The success of this method depends on a fine grid of stellar masses along the isochrone. The isochrone method is more common of the two approaches and the one we will use.

The EPS models are dependent on the contemporary stellar evolutionary models. The incomplete understanding of certain stellar processes such as the convection in stellar interiors and some advanced phases of stellar evolution lead to uncertainties in the EPS models. Until recently, the lack of proper modeling of the post-main sequence asymptotic giant branch (AGB) phase was one of these factors limiting the reliability of the models. During the AGB phase the stars evolve into red giant domain and experience thermal pulses. These thermal pulses are complex to model but crucial in determining the surface properties of the AGB

stars and consequently the effect on the photometric properties of the population. Despite its transient, relatively short-lived nature, the AGB phase does have a considerable impact on the integrated light of a population, especially in the infrared domain. In this work I shall investigate the effects that the improved AGB models (Marigo et al., 2008) have on the integrated photometric properties of stellar populations.

Mass is a critical quantity in many problems of astrophysical interest. Its measurement however requires indirect means that commonly relate the kinematics of the object to spectroscopic observables. The theoretical mass-to-light–color (MLC) relations offer an alternative approach to the problem. The concept was first introduced by Bell and de Jong (2001). They showed, based on population synthesis models, that there is a tight correlation between (certain) colors of a galaxy and its mass-to-light ratio. Thus it is possible recover the stellar mass (both in living stars and in remnants) from the photometric properties of the population. MLC relations have been widely adopted in practice: Kassin et al. (2006) and Kranz et al. (2003) implemented the MLC relations provided by Bell and de Jong to quantify dark matter contribution to spiral galaxy dynamics while Bakos et al. (2008) used the MLC relations for the SDSS passbands by Bell et al. (2003) when exploring radial color and stellar surface mass density profiles for a sample of spiral galaxies, just to mention a few examples.

Nowadays, mass estimates are typically conducted in the near-infrared, because these wavelengths are less prone to the effects of recent bursts of star formation and dust attenuation and because of the availability of extensive photometric libraries based on near-IR surveys. However, one must also notice that the near-IR regime is also heavily affected by the AGB stars in the population. Therefore, in order to provide robust MLC relations in the near-IR, one must include a detailed description of the AGB phase in the population synthesis models. Hitherto, only a handful of EPS models have managed to incorporate a proper treatment of the AGB phase. Therefore. the main goal of this work is to provide updated mass-to-light–color (MLC) relations for populations with extended star formation histories and with AGB phase being properly accounted for.

Besides recent advances in modeling the AGB phase, progress has been made in modeling the effects of interstellar dust on the integrated light of galaxies. We shall implement an attenuation model by Tuffs et al. (2004) and investigate its effects on our galaxy models and especially on the MLC relations. Bell and de Jong (2001) suggested that dust has little

effect on the MLC relations: the dimming of a galaxy is compensated by an equal amount of reddening in color, thus effectively canceling each other out. We shall see if this is still the case with the updated models for attenuation and AGB phase contribution to the integrated light.

The text is organized as follows. In Section 1 I will review the concept of a simple stellar population and discuss the properties of different initial mass functions and the impact the choice of an IMF has on the results. I will also describe evolution of the thermally pulsing AGB phase and discuss the impact that AGB stars have in a simple stellar population. In Section 2 I will present the results of the SSP model calculations based on the Padova stellar isochrones incorporating improved AGB models and compare these result with the older models. I will also discuss the importance of including circumstellar dust recipes in the EPS models for the purposes of this work. In Section 3 the SSPs are used to model populations with exponential star formation histories. I will compare our model results with a model presented in the literature (Bell and de Jong, 2001) to punctuate the importance of the proper treatment of the AGB phase in EPS models. I will also provide the updated MLC relations at Johnson-Cousins, 2MASS and SDSS bands. Section 4 deals with the effects of interstellar dust: simple model spiral galaxies are constructed for which dust attenuation effects are calculated according to the prescriptions by Tuffs et al. (2004) to investigate the importance of proper dust treatment in the near-infrared bands. Some concluding thoughts are presented in Section 5.

1 Simple stellar populations

1.1 Introduction to simple stellar populations

One of the basic approaches to theoretical stellar population synthesis is to make use of the simple stellar populations. SSPs are defined as stellar populations that are formed in a single instantaneous burst of star formation from a cloud of uniform metallicity. In other words the SSPs are assemblies of coeval and chemically homogeneous single stars that only differ in mass. The stellar masses of the population are assumed to follow a certain distribution called the Initial Mass Function (IMF), for example, a power law function of the mass. The initial mass function is usually normalized to a certain value so that

$$\int_0^\infty m\Phi_N(m)dm = M_{tot} \quad \text{and} \quad dN = \Phi_N(m)dm,$$

where dN is the number of stars within $[m, m + dm]$, Φ_N is the initial mass function (number density of stars as a function of mass) and m is the stellar mass. In this work all the IMFs are normalized so that the total mass of the IMF equals one, that is

$$\int_{0.1}^{100} m\Phi_N(m)dm = 1.$$

The photometric properties of a SSP can be calculated using sets of theoretical isochrones. The isochrones are constructed by interpolating the theoretical stellar evolutionary tracks and transforming those into a grid of masses of specific age. These isochrones have been tested and verified with observations in the solar neighborhood and star clusters. Figure 1 shows examples of stellar evolutionary tracks and isochrones in the HR diagram (Girardi et al., 2000). The chemical composition is the same for both the stellar tracks and the isochrones: helium abundance Y=0.23 and metallicity Z=0.0004. The stellar tracks on the left panel show the temporal evolution of stars for a range of masses (1.8 - 7.0 $M_\odot$) from the zero age main sequence to the TP-AGB phase, including a couple of thermal pulses in the model. The right panel shows the corresponding isochrones obtained from the stellar tracks. The isochrones are not derived solely from the tracks presented, stellar tracks down to 0.15 $M_\odot$ have been used to construct the isochrones. The two figures look very much alike, and the characteristic shapes in the tracks can also be found in the isochrones. The difference is that along the isochrones the running variable is mass rather than time.

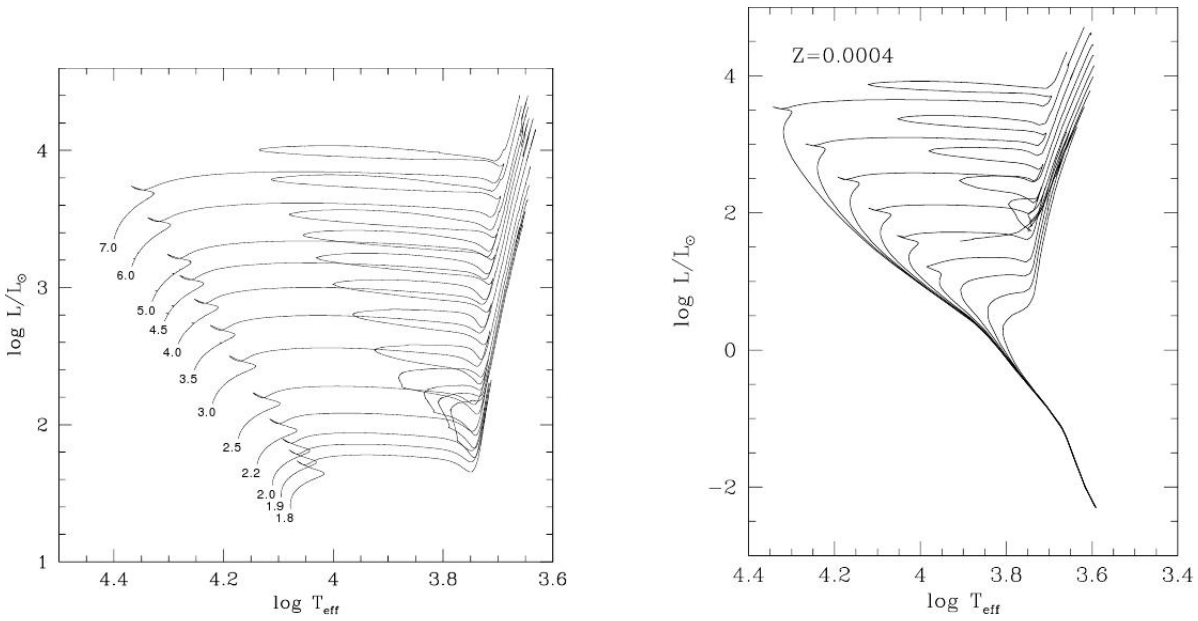

Figure 1: *Left panel:* Stellar evolutionary tracks in the HR diagram, for the composition [Z=0.0004, Y=0.23] The tracks are drawn up to the beginning of the TP-AGB phase. The initial masses are given at the beginning of each track. *Right panel:* Theoretical stellar isochrones in the HR diagram, for the composition [Z=0.0004, Y=0.23]. The age ranges from $\log(t/\mathrm{yr}) = 7.8$ to 10.2 (from top to bottom), at intervals $\Delta \log t = 0.3$. The main sequence is complete down to 0.15 $M_\odot$. From Girardi et al., A&AS, 141, 371, 2000, reproduced with permission © ESO.

For a SSP of given age t we have the luminosity at a wavelength λ

$$L_\lambda^{\mathrm{SSP}}(t) = \int_0^\infty \Phi_N(m) L_\lambda(m,t) dm, \tag{1}$$

where L_λ is the luminosity along the isochrone at wavelength λ. Typically the isochrone tables are provided with magnitudes in a given photometric system. Using these magnitudes, one gets the luminosity of a SSP in equation 1 for a certain band, rather than for a specific wavelength.

Mass-to-light ratios

An interesting quantity for stellar populations is the mass-to-light (M/L) ratio. This quantity reflects the ratio between the total mass in stars and stellar remnants and the luminosity output of the population in solar units. Naturally this quantity changes with time as stars complete

their evolution changing the total mass (in stars and remnants) and luminosity of the population. In order to calculate the M/L ratio for different epochs we need to know the time evolution of both the mass in stellar objects and the luminosity of the population. The latter comes out naturally using equation 1 and scaling the output to solar units. To find out the mass locked in stars and remnants, we need to know the amount of gas that stars return to the interstellar medium by the end of their lives. For this we define the returned gas fraction R, according to Tinsley (1980), by the integral

$$R(t) \equiv \int_{m_t}^{\infty} (m - w_m)\Phi_N(m)dm,$$

where m_t is the turnoff mass for the given age and w_m is the remnant mass for a star of initial mass m. The turnoff (TO) mass is the lowest mass for a star that has evolved off the main sequence (MS) by the given time T. The post-main sequence (PMS) phase is considerably shorter that the MS and as an approximation, the turnoff age can be considered to be the final age of the star and the moment of remnant formation. The mass locked in stars and remnants in the population is then

$$M_*^{\mathrm{SSP}}(t) = 1 - R(t) = 1 - \int_{m_t}^{\infty} (m - w_m)\Phi_N(m)dm. \quad (2)$$

Now (with the knowledge of remnant masses for different initial masses) we can calculate the M/L ratios for SSPs with varying ages using the equations 1 and 2.

1.2 Initial mass functions

The choice of an initial mass function has an effect on the photometric properties of a stellar population, since the properties of stars depend heavily on their masses. In order to simulate the photometric evolution of a SSP, we need to determine the number distribution of stars forming with different masses. There are plenty of IMFs in the literature based on surveys of the solar neighborhood, star clusters and nearby galaxies. It is beyond the scope of this thesis to present the results with a wide range of initial mass functions and thus one IMF has to be chosen and we need to choose an IMF that best suits our purposes. The choice of a specific IMF does not cause crucial changes in the output of our models. For example, in this work we are interested in the mass-to-light–color correlation; the choice of a IMF does affect the

absolute value of the mass-to-light ratio calculated for SSPs and more complex models, but does not change the general trend of M/L-color correlation. This is natural as an IMF with a lot of weight in the low mass range of stars hardly changes the global luminosity or the colors of the population, but has a significant effect on the total mass. So changing the IMF only results in a shift in the zero point, as discussed by Bell and de Jong (2001).

As one major goal of this work is to point out the importance of the TP-AGB phase in stellar population synthesis, we shall pick an IMF that can help to accentuate this. For this, we shall define the following quantities

$$\zeta \equiv \frac{\int_1^{100} \Phi(m)dm}{\int_{0.1}^{100} \Phi(m)dm}, \quad \Phi(m) = m\Phi_N(m)$$

$$\zeta_n \equiv \frac{\int_1^{n} \Phi(m)dm}{\int_{0.1}^{100} \Phi(m)dm}$$

The range of the integral in the divider comes from the mass range used in our IMFs presented below. The range in the dividend is chosen to represent the stars that contribute most to the total light, and thus stars with masses below solar are neglected. Because we have normalized our total IMF mass to one, we have

$$\zeta = \int_1^{100} \Phi(m)dm$$

and

$$\zeta_n = \int_1^{n} \Phi(m)dm.$$

For the stellar evolutionary tracks used, stars within range $1\,\mathrm{M}_\odot < m \leq 5\,\mathrm{M}_\odot$ undergo an AGB phase during their lifetimes. Therefore it is interesting to compare the quantity ζ_5/ζ for different initial mass functions. This quantity displays the relative importance of the AGB phase for the IMF. The higher the value is, the larger is the number of stars in this mass range and hence the bigger is the contribution to the integrated light. In other words, the luminosity of AGB stars versus the total luminosity of stars with masses above solar is proportional to the ratio ζ_5/ζ:

$$\frac{L_{\mathrm{AGB}}}{L} \propto \frac{\zeta_5}{\zeta}.$$

IMF	ζ	ζ_5	ζ_5/ζ
Salpeter	0.393	0.211	0.537
Kroupa 1998	0.405	0.285	0.706
Kroupa 2001	0.380	0.194	0.510
Chabrier	0.545	0.324	0.594
Arimoto and Yoshii	0.666	0.233	0.350

Table 1: Comparison of IMF quantities. ζ gives the ratio of "heavy" stars. ζ_5/ζ gives the relative contribution of stars that experience the AGB phase.

Let's look at some of the commonly used IMFs: an extended Salpeter (1955), Arimoto & Yoshii (1987), Kroupa98 (1998), Kroupa01 (2001), and Chabrier (2001). All the IMFs include stellar masses from 0.1 $M_\odot$ to 100 $M_\odot$, except Chabrier which goes down to 0.01 $M_\odot$. The coefficients given are determined by our normalization that sets the total mass of an IMF to one solar mass.

$$\Phi(m)_{\rm salp} = Cm^{-1.35} \qquad C = 0.1716$$

$$\Phi(m)_{\rm ay} = \frac{C}{m} \qquad C = 0.1448$$

$$\Phi(m)_{\rm kr98} = \begin{cases} Cm^{-0.5} & m < 0.5 \\ Dm^{-1.2} & 0.5 \le m < 1 \\ Dm^{-1.7} & m \ge 1 \end{cases} \qquad C = 0.4799,\ D = 0.2954$$

$$\Phi(m)_{\rm kr01} = \begin{cases} Cm^{-0.8} & m < 0.5 \\ Dm^{-1.7} & 0.5 \le m < 1 \\ Dm^{-1.3} & m \ge 1 \end{cases} \qquad C = 0.2841,\ D = 0.1522$$

$$\Phi(m)_{\rm chab} = Cm^{-2.3} \exp\Big[-\Big(\frac{m_c}{m}\Big)^{1/4} \Big] \qquad C = 40.33,\ m_c = 716.4$$

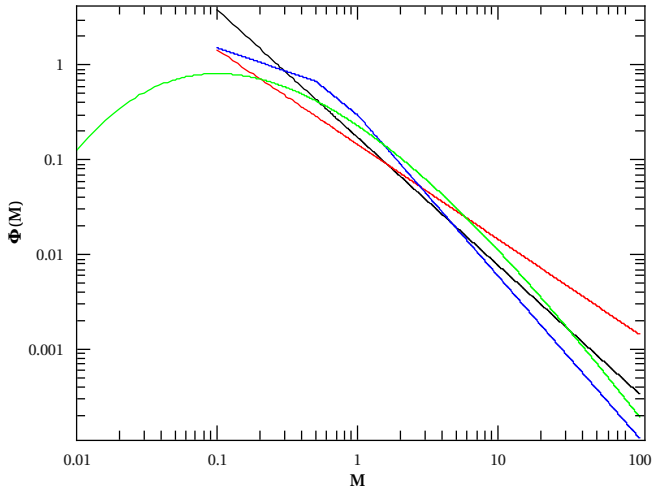

Figure 2: Four IMFs presented for comparison. Salpeter (black line), Kroupa98 (blue) and Arimoto & Yoshii (red) represent power law IMFs, while Chabrier (green line) is the only exponential IMF in our study.

The ζ values and ζ_5/ζ ratios for IMFs mentioned are summarized in Table 1. Each of the IMFs listed above are used to describe certain types of stellar populations. The Kroupa 1998 IMF is found to represents well the IMF of the Solar neighborhood. It also has the highest ζ_5/ζ ratio and thus it is chosen to be our preferred IMF. It is used implicitly in this work unless specified otherwise.

In Figure 2 there are four IMFs plotted for visualization and comparison: Salpeter, Arimoto & Yoshii, Kroupa98 and Chabrier. From this figure it is clear to note that the traditional Salpeter IMF contains most stars in the low end of the mass range. On the other hand, due to its shallow slope, the Arimoto & Yoshii IMF has more weight in the high mass range than the rest of the IMFs. The relative importance of the AGB phase (ζ_5/ζ ratios) can be understood qualitatively based on the plot. The highest contribution in the 1 to 5 $M_\odot$ range (and highest ζ_5) is shared with two IMFs: Kroupa98 and Chabrier. Arimoto & Yoshii is first to be ruled out of the comparison, because of the high contribution of massive stars and therefore high ζ. Of the remaining three, the Kroupa98 IMF has clearly the lowest contribution in the $M \gtrsim 5$ $M_\odot$ range resulting in the best ratio. Of course this kind of evaluation is not very solid without calculations, but it provides a way to visualize the zeta ratios.

1.3 Stellar masses and outline of stellar evolution

The classification of stars into mass intervals is based on the physical processes behind stellar evolution. The mass limits are slightly model-dependent. This classification scheme is based on the stellar models from the Padova group in which the convective overshoot is adopted. The effect of convective overshoot to the classification is that it lowers the mass limits for low- and intermediate-mass stars compared to the standard models (Chiosi et al., 1992; Iben, 1991).

Low-mass stars are those that after main sequence develop an electron degenerate helium core. When the helium core mass gets high enough, a He-burning runaway is initiated (the helium flash). The stars then develop degenerate CO-cores and enter the AGB phase. The AGB phase is terminated by the loss of the envelope by stellar wind and the stars become white dwarfs. The maximum initial stellar mass for the He-flash to occur ($M_{\rm HeF}$) is considered as the maximum mass for the low-mass class of stars. This mass is about 1.6 - 1.7 $M_\odot$ (1.8 - 2.2 $M_\odot$ for standard models), depending on the initial chemical composition.

Intermediate-mass stars ignite helium in non-degenerate conditions and develop a degenerate CO-core. The evolution then follows a path similar to that of low-mass stars - they undergo the AGB phase, lose mass by stellar wind and end up as white dwarfs. The upper limit for intermediate stars is defined by the minimum initial mass for which carbon ignition in non-degenerate conditions can occur ($M_{\rm up}$). This corresponds to about 5 $M_\odot$ (about 8 $M_\odot$ for standard models), the exact mass depending on chemical composition.

Quasi-massive stars in the range $\sim$ 6 to 8 $M_\odot$ undergo core carbon burning in non-degenerate conditions and develop highly degenerate O-Ne-Mg-cores. They become dynamically unstable to electron capture and explode as supernovae or end up as O-Ne-Mg white dwarfs.

Massive stars with masses higher than 8 $M_\odot$ suffer from mass loss by stellar wind throughout their whole evolutionary history. These stars form an iron core with material in less advanced burning stages in surrounding shells all the way to hydrogen-rich outer envelope. These stars end their lives as supernovae that are triggered by core collapse induced by e-captures on heavy nuclei, photo-dissociation of Fe into α-particles and rapid neutronization of the collapsing material. Either a neutron star of about 1.4 $M_\odot$ or a black hole of larger mass is left over, depending on the efficiency of neutrino cooling during the previous stages.

1.4 TP-AGB phase in stellar evolution

Before the AGB phase, a star has undergone a series of evolutionary stages in which first hydrogen and then helium have been exhausted from the stellar core. The details of this evolution vary with stellar mass, but the exhaustion of central helium marks the beginning of the early-AGB (E-AGB) phase. At this stage the star is composed of a degenerate CO-core with a He-burning shell surrounding the core and a hydrogen-rich envelope with a H-burning shell at its base. When helium is depleted in the central regions, the carbon-oxygen core contracts and rapidly heats up causing the envelope to expand and cool down. This terminates the hydrogen burning in the shell at the base of the envelope. This allows the convective envelope to reach inwards in mass. For massive enough stars ($M \gtrsim$ 3 - 3.5 $M_{\odot}$, for models without and with convective overshoot) (Izzard et al., 2004; Girardi et al., 2000) the convection can penetrate into regions of recent hydrogen burning, transporting fresh CNO products like helium and nitrogen to the surface. This is called the second dredge-up. The contraction of the core is halted when the density is high enough for electrons to become degenerate. Eventually, the envelope cools down, re-contracts and causes temperature to rise at its base until hydrogen is reignited in a thin shell. This is when the early-AGB ends and the Thermally Pulsing AGB (TP-AGB) phase begins.

The temperature in the degenerate CO core reaches about 10^8 K, which is high enough to ignite helium in a thin shell above the core, but below carbon ignition temperature. During the TP-AGB phase shell hydrogen burning and shell helium burning alternate. The hydrogen burning shell is the main source of energy for about 90 per cent of the time while the helium burning shell is inactive. Hydrogen burning accumulates helium in the inter-shell region until the conditions at the base of this region force a thermonuclear runaway by triple alpha process. This helium shell flash heats the surrounding material and forces the envelope to expand and consequently temporarily extinguishes the hydrogen burning shell. The helium burning shell also expands and cools ending the runaway burning. Once relaxed, helium burning continues quiescently in a thin shell until helium is exhausted. The quiescent helium burning last about 10 per cent of the time between successive flashes. Once helium burning ends, the envelope contracts once again and the hydrogen burning shell reignites completing the cycle. The cycle

duration depends on the mass of the core (Paczynski, 1975):

$$\log(T_{\rm P}) \approx 3.05 + 4.5\Big(1 - \frac{M_C}{\rm M_\odot}\Big) \quad \text{yr.}$$

In practice, the core mass never reaches the theoretical upper limit of 1.4 $M_\odot$, the highest value for the core mass in the models is about one solar mass. Thus the cycle duration ranges from around one thousand years for the most massive stars (core mass $\sim$ 1.0 $M_\odot$) to some 10^5 years for the lowest mass stars. The duration of the whole TP-AGB phase is in the order of 10^6 years. The total number of flashes for the least massive AGB stars varies around 10. For the most massive AGB stars, the number of flashes reaches a few hundred, with a slight dependence on the chemical composition.

During the helium flash, a thin convective layer is formed above the helium burning shell. This layer mixes some of the helium burning "ashes" (carbon from the triple alpha process) into the inter-shell region. The convective layer disappears as the quiescent helium burning commences. After the helium shell runs out of fuel and before the hydrogen shell reignites, the outer convective envelope might reach deep enough to bring carbon from the inter-shell region to the surface. This is called the third dredge-up. The occurrence of carbon stars (with C/O > 1, where C and O are the abundances of carbon and oxygen in the photosphere) is a result from a series of third dredge-up events bringing carbon to the surface. There is another mechanism that affects the formation of carbon stars, the hot-bottom burning (HBB). If the hydrogen-rich envelope is massive enough, the base of the envelope can get hot enough so that nucleosynthesis (CNO cycle) occurs at the bottom of the convective envelope itself, hence the term hot-bottom burning. HBB occurs in stars with initial masses between 3.5 and 4.5 $M_\odot$, depending on metallicity (Marigo and Girardi, 2007). HBB nucleosynthesis can cause depletion of freshly dredged-up carbon by converting it into nitrogen. This can delay or prevent the formation of C stars. On the other hand, with low-metallicity, the temperature at the base of the envelope can reach high enough temperatures to activate the ON cycle which causes destruction of oxygen and formation of nitrogen instead. In this case, HBB acts in favor of carbon star formation (Ventura et al., 2002).

In Figure 3 we can see the schematic structure of an AGB star. The He- and H-burning shells are separated by an inter-shell region consisting mainly of helium ($\sim$ 75%) and carbon ($\sim$ 22%) with some neon and oxygen. Areas of flash-driven convection and third dredge-up convection are indicated on top of the diagram. Note that the diagram is not to scale. For

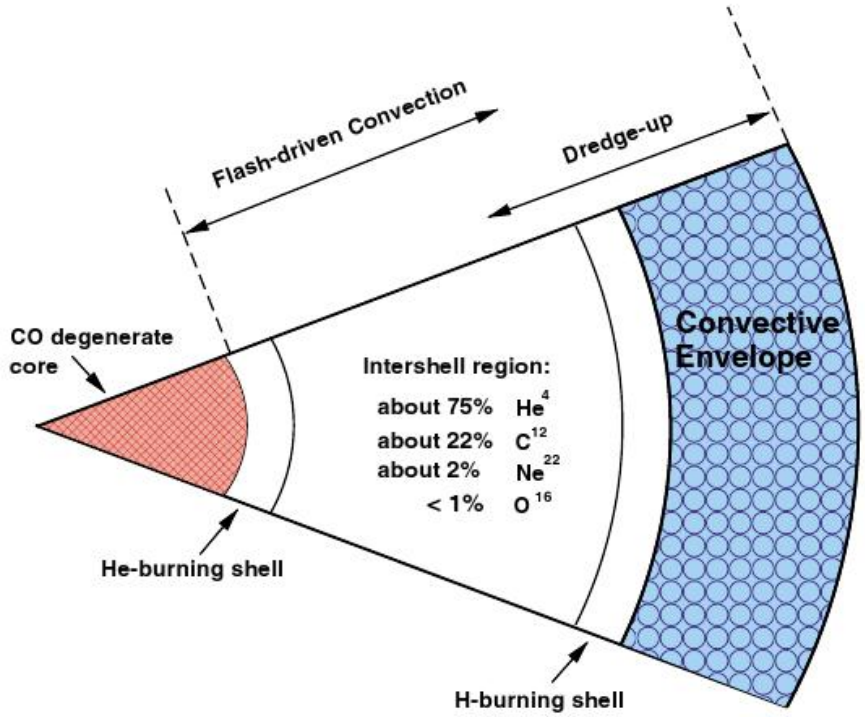

Figure 3: Schematic structure of an AGB star. The diagram is not to scale - the helium burning and hydrogen burning shells as well as the inter-shell region are substantially less extensive in a real star. From Karakas et al. (2002). Courtesy Csiro Publishing, http://www.publish.csiro.au/nid/138/paper/AS02013.htm.

example, the radial thickness of the hydrogen-rich envelope is about 1×10^5 times larger than the thickness of the hydrogen burning shell.

During the TP-AGB phase each cycle increases the CO core mass due to helium burning. On the other hand the envelope mass decreases due to hydrogen burning (and consequent helium burning) and also because of mass loss in stellar winds. The mass loss rate increases with increasing luminosity, which in turn increases with core mass. As a consequence, most of the mass loss occurs at the end of the AGB phase. Eventually the whole envelope will be blown out unveiling the CO core and leaving a CO white dwarf behind. The ejected envelope forms a planetary nebula.

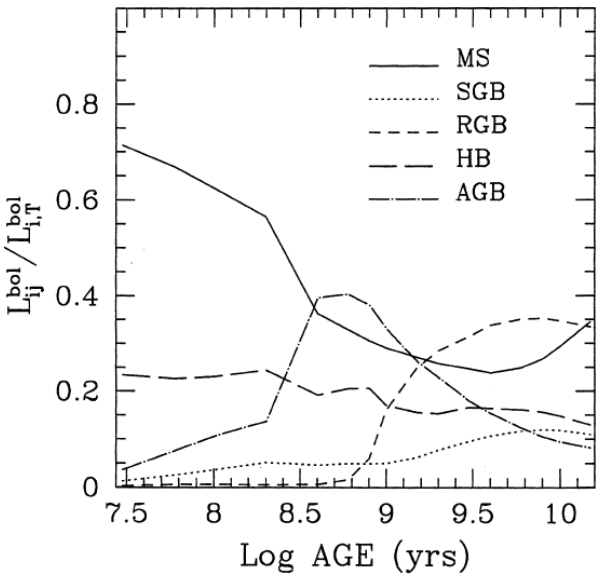

Figure 4: The time evolution of the relative contributions of bolometric light of various stellar evolutionary stages to the total bolometric light of a SSP. The abbreviations denote to main sequence (MS), sub-giant branch (SGB), red giant branch (RGB), helium burning stages (HB) and asymptotic giant branch (AGB). From Maraston (1998).

1.5 TP-AGB phase in stellar populations

The age of a SSP is the most important quantity affecting the integrated magnitudes in different bands. The youngest SSPs contain massive main sequence stars that dominate the luminosity over a wide spectral range with a contribution from the post-main sequence helium burning stars. As the population grows older, the MS stars still typically present a major contribution to the bolometric luminosity and to the luminosity in optical bands, but the PMS contribution increases gradually. The most important PMS stage for intermediate mass stars is the asymptotic giant branch. The onset of the AGB occurs at around 10^8 yr, corresponding to a turnoff mass of 5 $M_\odot$. The AGB phase contribution to the integrated light of the population for the current models will be discussed in Section 2.2. The red giant branch (RGB) dominates the PMS luminosity for low mass stars at SSP ages $\sim 10^9$ yr and above with TO mass equal to or less than $M_{\rm HeF}$ (1.6 - 1.7 $M_\odot$).

The importance of the AGB phase in population synthesis has been emphasized by several

authors. Maraston (1998) showed that the AGB phase dominates the luminosity output in simple stellar populations with ages between 0.3 and 2 Gyr (see Figure 4). The AGB phase provides 40 per cent of the bolometric luminosity in stellar populations of intermediate age and up to 80 per cent of the luminosity in the near infrared. Similar results were obtained by Frogel et al. (1990) when they observed clusters in the Magellanic clouds. The contribution of the TP-AGB phase to the bolometric luminosity peaked at 40 per cent in the intermediate age ($\sim$ 2 Gyr) clusters.

Despite the obvious impact of the TP-AGB phase to the integrated colors and magnitudes, most of the population synthesis models presented in the literature do not account for the TP-AGB phase in enough detail, due to the complexity of the TP-AGB phase modeling. The TP-AGB phase has been taken into account by some authors, but some recent advances in modeling certain aspects of this evolutionary phase, namely the third dredge-up with formation of carbon stars, the effects of hot bottom burning and variation of molecular opacities along the TP-AGB evolution have not been included in most of these models. Marigo et al. (2008) (the Padova library) have provided updated isochrones in which these recent improvements have been accounted for, making the Padova set of isochrones probably the most up-to-date in the field of AGB phase modeling. These isochrones have been calibrated to reproduce the basic observables of AGB stars in the Galaxy and the Magellanic Clouds.

2 SSP models

2.1 Datasets

This work makes use of the isochrones of the Padova group. The isochrones have been obtained using the CMD 2.2 web interface maintained by Leo Girardi at the Astronomical Observatory of Padova. Two basic sets of isochrones were obtained: one based on Marigo et al. (2008) (hereafter the 2009 dataset, or the "new" dataset) and another based on Girardi et al. (2002) (hereafter the 2002 dataset, or the "old" dataset). The 2002 dataset uses only a simplified description for the thermally pulsing AGB phase, while the 2009 dataset implements more detailed and calibrated TP-AGB phase models. Therefore we expect to see some differences between SSPs calculated using the 2002 and 2009 datasets, especially in the near infrared bands, and differences with respect to results in the literature using different recipes for TP-AGB or none at all.

Isochrone ages range from $\log(t/\mathrm{yr}) = 6.0$ to 10.2 with intervals $\Delta(\log t) = 0.05$. The isochrones were obtained for different photometric systems, namely the Johnson-Cousins *UBVRIJHK* and the Two Micron All Sky Survey (2MASS) JHK_s bands for both 2002 and 2009 data sets. In addition the 2009 data set also includes isochrones for the Sloan Digital Sky Survey (SDSS) filters. The reason for omitting SDSS tracks for the 2002 data set is that there are only slight differences in the integrated light in the optical region with respect to 2009, as seen from the comparison made in *UBVRI* bands. Seven metallicities were selected, ranging from 0.0001 to 0.03. The metallicities and corresponding color coding can be found in Table 2. All the plots in this work will be displayed so that one color will always represent a certain metallicity as outlined in the provided table unless noted otherwise.

A FORTRAN code was used to calculate the integrated magnitudes (according to equation 1) and mass-to-light ratios as a function of SSP age. For calculating the mass-to-light ratios, returned gas fractions from Portinari et al. (1998) were used.

2.2 AGB phase contribution to the integrated light

As already discussed in section 1.5, the light emitted by AGB stars in a SSP of intermediate age can have a significant contribution to the total luminosity output of the population. In

Table 2: List of metallicities used in this work and the corresponding colors used in plots.

Z	Figure color
0.0001	cyan
0.0004	yellow
0.001	orange
0.004	blue
0.008	green
0.019	red
0.03	black

Figure 5 we can see the relative contributions of the AGB phase *K*-band and bolometric luminosities against the total luminosities of a simple stellar population calculated for the 2009 dataset. We can see that in the *K*-band, the AGB contribution peaks at about 90% for a very low metallicity model (Z=0.0001). For models with higher metallicities, the *K*-band ratio peaks at 65% and above. The bolometric ratio peaks around 45% for Z=0.008, while for rest of the metallicities the peak AGB contribution ranges between 30 - 40%. In general, the relative contribution of the AGB phase is at its most prominent around 0.3 - 1 Gyr. These results are in good agreement with the discussion in section 1.5 and with Figure 4.

At low metallicities, the stars enter the AGB phase at slightly higher luminosities than at higher metallicities. The hot-bottom burning provides a higher increase in luminosity with lower metallicities (Izzard et al. 2004 eq. 32). Therefore the bolometric ratio for low-Z models ($Z \lesssim 0.0004$) raises rapidly to high values at the onset of the AGB phase. The significant leap in the AGB luminosity ratio in the *K*-band at low metallicities is a result of the formation of carbon stars. As noted already by Renzini & Voli (1981), the lower the metallicity, the lower is the amount of oxygen present in the envelope and therefore less carbon has to be dredged-up in order to achieve C/O > 1. This means that a smaller number of dredge-up episodes is required to produce carbon stars. According to the 2009 model recipes (Marigo and Girardi, 2007), the onset of the third dredge-up in stellar models of any mass would take place since the first thermal pulse for metallicities $Z \lesssim 0.001$. As a consequence, the

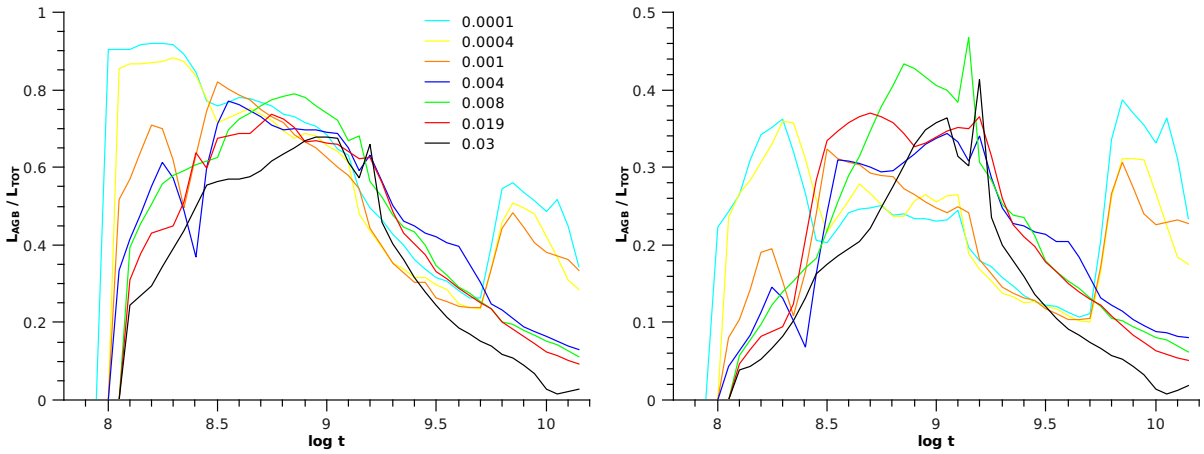

Figure 5: Relative contributions of the AGB phase luminosity versus the total luminosity of a SSP using the 2009 dataset. The ratios are plotted as a function of time, with metallicities listed on the left panel. The odd behavior of low metallicity models at ages $\log(t) \gtrsim 9.7$ is explained in the text. *Left panel:* K-band ratios. *Right panel:* Bolometric ratios.

formation of carbon stars in a metal-poor population will take place very soon after the onset of TP-AGB phase, implying larger K-band luminosities. The impact of metallicity on carbon star formation is clearly presented in Figure 6 taken from Marigo et al. (2008). The left panel displays isochrones for Z=0.0001. It can be seen that once the stars enter the TP-AGB phase, the carbon-rich configuration, depicted with red color in the diagram, dominates almost the whole range of masses (ages) down to the lowest masses, where the oxygen-rich configuration gains some foothold. The situation is very different in the right panel, showing isochrones for Z=0.008. Both the high- and low-mass ends evolve completely in the O-rich domain, while in the middle range, the stars do evolve into C-rich configurations.

In Figure 5 we can also see some strange behavior for low-Z ($Z \lesssim 0.001$) models with ages $\log t = 9.8$ and above. Here the ratio suddenly takes a turn to higher values. The reason behind this unexpected behavior lies in the mass loss formulation adopted, which does not work very well at low metallicities leading to lower mass loss rates. This in turn leads to higher luminosities for the metal-poor models and to the observed increase in the AGB luminosity contribution. In addition to the mass loss formulation itself, another factor has to be addressed. Because of the lack of observed carbon stars in Galactic globular clusters with initial masses $M < 1\ \mathrm{M}_{\odot}$, an artificial cut to the occurrence of the third dredge-up at one solar mass has been

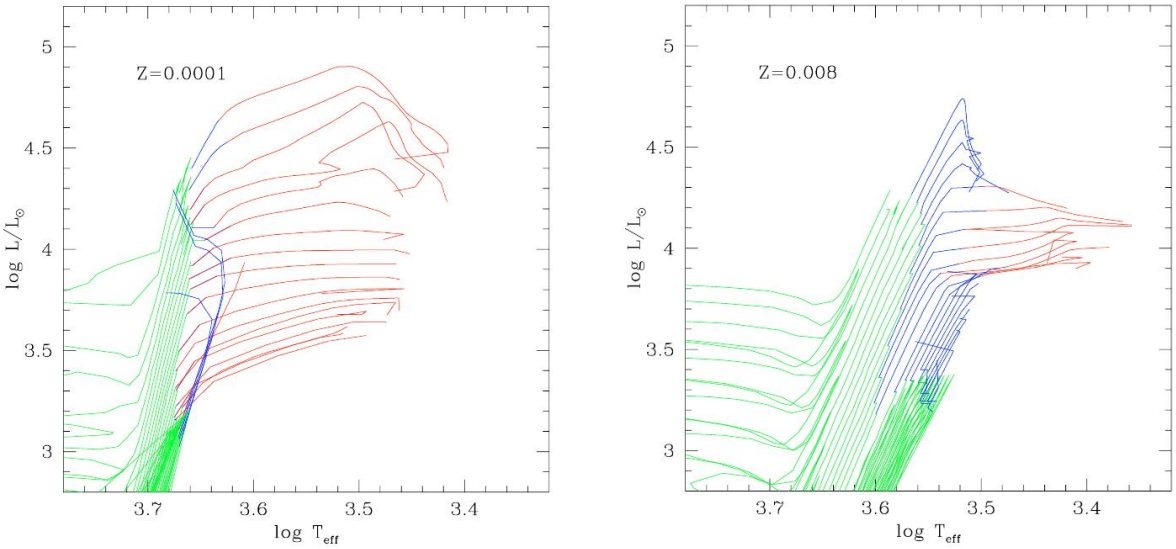

Figure 6: Isochrones in the HR diagram for two metallicities, zooming in the AGB phase. The isochrones are plotted with ages log(t/yr) = 7.8 to 10.2 (from top/left to bottom/right) with a spacing of 0.1 dex in log t. The pre-TP-AGB phases are drawn in green, while blue and red lines correspond to surface O-rich and C-rich phases of the TP-AGB. From Marigo et al., A&A, 482, 883, 2008, reproduced with permission © ESO.

introduced (Marigo and Girardi, 2007). The non-occurrence of the third dredge-up for stars with low Z and mass below 1 $M_\odot$ leads to substantially lower mass-loss rates than for stars with higher intrinsic metallicity. This effect can be seen in the left panel of Figure 6. The older isochrones evolve in the O-rich configuration seen as blue lines starting from the bottom right part of the isochrone bunch. These isochrones lead to higher luminosities than do the ones that are closest to the O-rich tracks, but evolve into the C-rich configurations.

It is good to keep in mind that this effect results from model limitations and is not observable in real stellar populations. As we later turn to examine stellar populations with extended star formation histories, the interest in these low metallicities will be diminished as we will examine 10 Gyr old galaxies which very seldom display such low metallicities due to internal metal enrichment. We shall also note that the problems with low-Z mass loss formulation has been acknowledged and improved mass loss prescriptions for the low metallicity stars are currently being implemented for the Padova library (private communication). These new models will be tested against the luminosity function of white dwarfs in the Galactic halo.

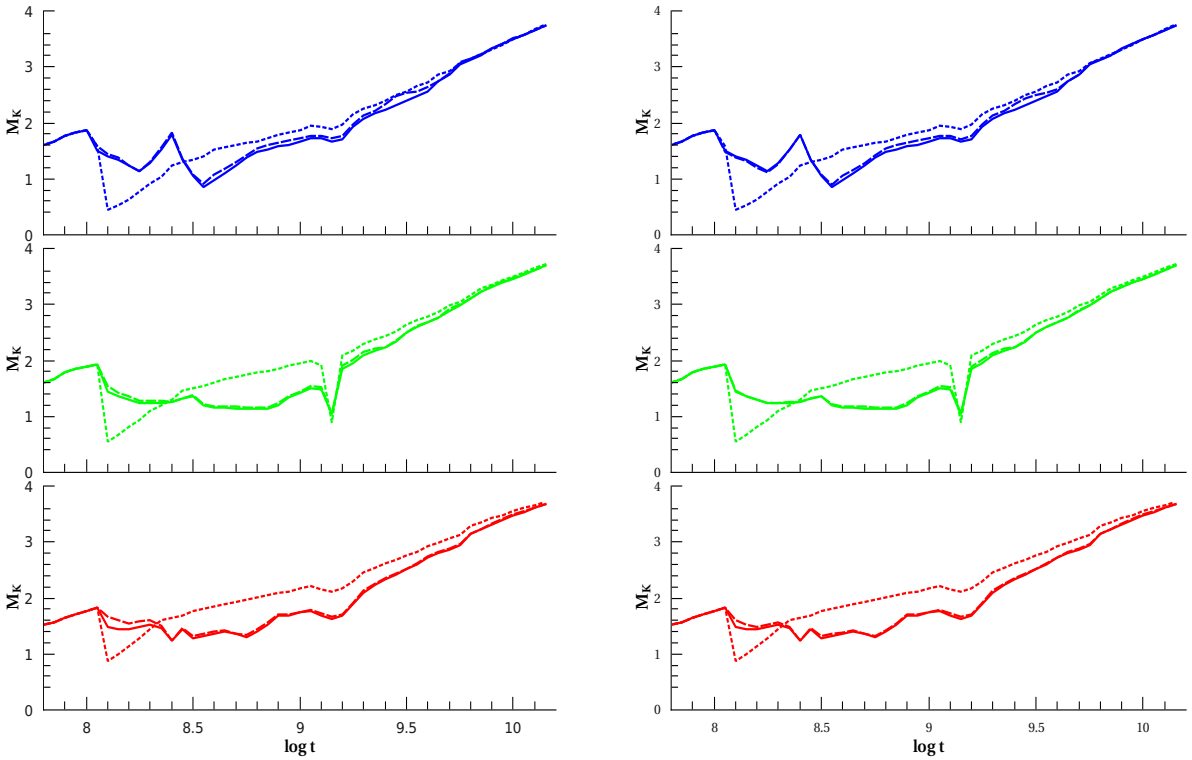

Figure 7: The effect of circumstellar dust in a SSP. K-band magnitude versus SSP age for three metallicities. The 2009 data set without dust is shown as a solid line and the same set with dust as dashed line. The dotted line refers to the 2002 data set (without dust). Bressan and Groenewegen models on the left hand side and right hand side respectively. *Top panels:* Z=0.004 *Middle panels:* Z=0.008 *Lower panels:* Z=0.019.

2.3 Circumstellar dust

The Padova group isochrones are also available with circumstellar dust around AGB stars being accounted for. This applies only in the case of Marigo et al. (2008) and later tracks, so circumstellar dust is not applicable in our 2002 data set. The circumstellar dust recipes follow either Bressan et al (1998) or Groenewegen (2006). The major consequence of introducing circumstellar dust in the stellar model is that a portion of the light radiated in optical bands gets reprocessed in the circumstellar envelope and re-emitted in the far infrared.

In Figure 7, a comparison between old and new SSP models with and without circumstellar dust is presented. On the left, the dust is composed of silicates for M stars and of graphites for

C stars according to the Bressan model. On the right, a Groenewegen model for circumstellar dust is adopted. In this case, the recipe for dust contains 40% silicates and 60% aluminum oxide for M stars and a combination of 85% amorphous carbon and 15% silicon carbide for C stars. The magnitude in K-band is plotted against logarithm of SSP age for three metallicities and three models: the 2002 data set (dotted line), the 2009 data set without circumstellar dust (solid line) and the 2009 data set with dust (dashed line). We can see from the figure that until the SSP age reaches about 100 Myr, all three models share a common magnitude evolution. This is the age when the AGB phase transition occurs. The difference between the 2009 SSPs with and without circumstellar dust is tiny in comparison to the difference between the old and the new models. In bluer bands the difference between the model containing dust effects and the dust-free model gets almost negligible while the difference between 2009 and 2002 models remains, but it is much smaller than in K-band. When plotted in U, B or V bands, the 2009 SSPs with and without dust coincide with each other and no difference can be seen. Also the difference with respect to the 2002 model is lost. The effect of different dust models do not differ much from each other. The Bressan formulation seems to produce a bit larger deviation from the dust-free models than the Groenewegen one. Next, we shall use the Bressan dust model to see how the circumstellar dust affects the mass-to-light ratio.

In Figure 8 we can see the mass-to-light ratio of a SSP at 2MASS K_s-band and with solar metallicity (Z=0.019). Between $\log(t/\mathrm{yr}) \sim 8.0$ and $\log(t/\mathrm{yr}) \sim 8.8$, the model incorporating dust results in slightly higher M/L ratios than the dust free one. However the difference is minor compared to the difference between 2002 and 2009 models. The dust effect is most prominent in K_s; the effect gets weaker moving towards bluer bands. The impact of dust does not change much if a different composition (Groenewegen) is adopted. In other words the impact of circumstellar dust on the integrated light of a stellar population is far less crucial than the improved treatment of the TP-AGB phase. The result is an expected one, since in a population of stars, the major contribution to luminosity in the optical regime, which is most prone to dust effects, comes from MS stars that do not contain much dust. The giant stars that do contain dust, having lower effective temperatures, radiate more efficiently at longer wavelengths and hence do not suffer from serious dust reprocessing. As a conclusion, the circumstellar dust can be neglected in the remainder of this work with confidence.

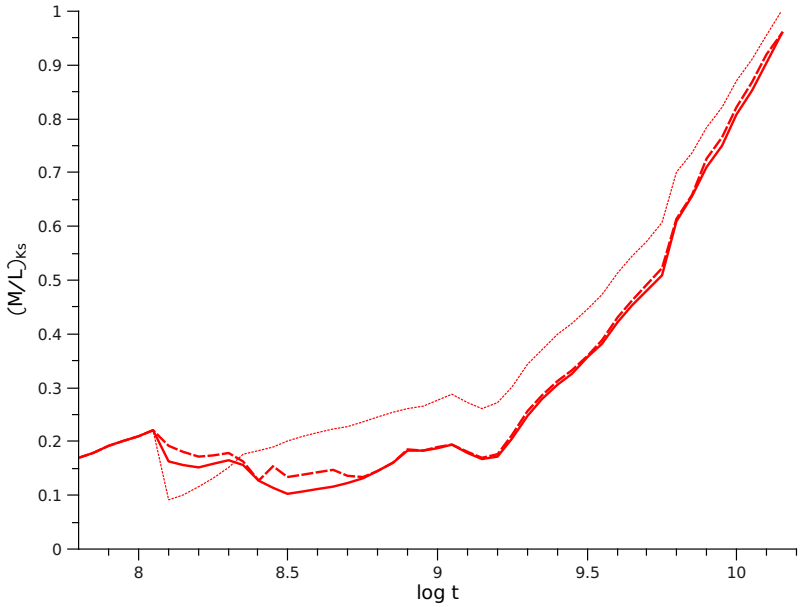

Figure 8: Mass-to-light ratios for a SSP of solar metallicity. Line styles as in Figure 7.

2.4 Interpreting the model results

2.4.1 The AGB phase transition and the time evolution of colors and mass-to-light

The AGB phase transition occurs when the population reaches an age at which the most massive stars in the population reach as low as $M_{\rm up}$. The evolution of stars above and below this limit follow quite different paths. Stars with $M > M_{\rm up}$ burn C and O in the core with no significant increase in the core mass $M_{\rm c}$. Below $M_{\rm up}$, the CO core is degenerate and the stars experience the AGB phase which usually results in an increase in $M_{\rm c}$ during the phase. It results in an increase in the nuclear fuel at a quite precise value of initial mass (Girardi and Bertelli, 1998). According to the Fuel Consumption Theorem by Renzini and Buzzoni (1986), the increase in nuclear fuel burned leads to an increase in the total luminosity of the population. As the increase occurs in red giant stars, the integrated SSP colors experience a jump to the red at the onset of the AGB phase.

In Figure 9 we can see some properties of SSP models calculated for both 2002 and 2009 datasets. Three metallicities were selected from a very metal poor Z=0.0001 model to Z=0.004 and 0.019 models representing metallicities typical to the Small Magellanic Cloud

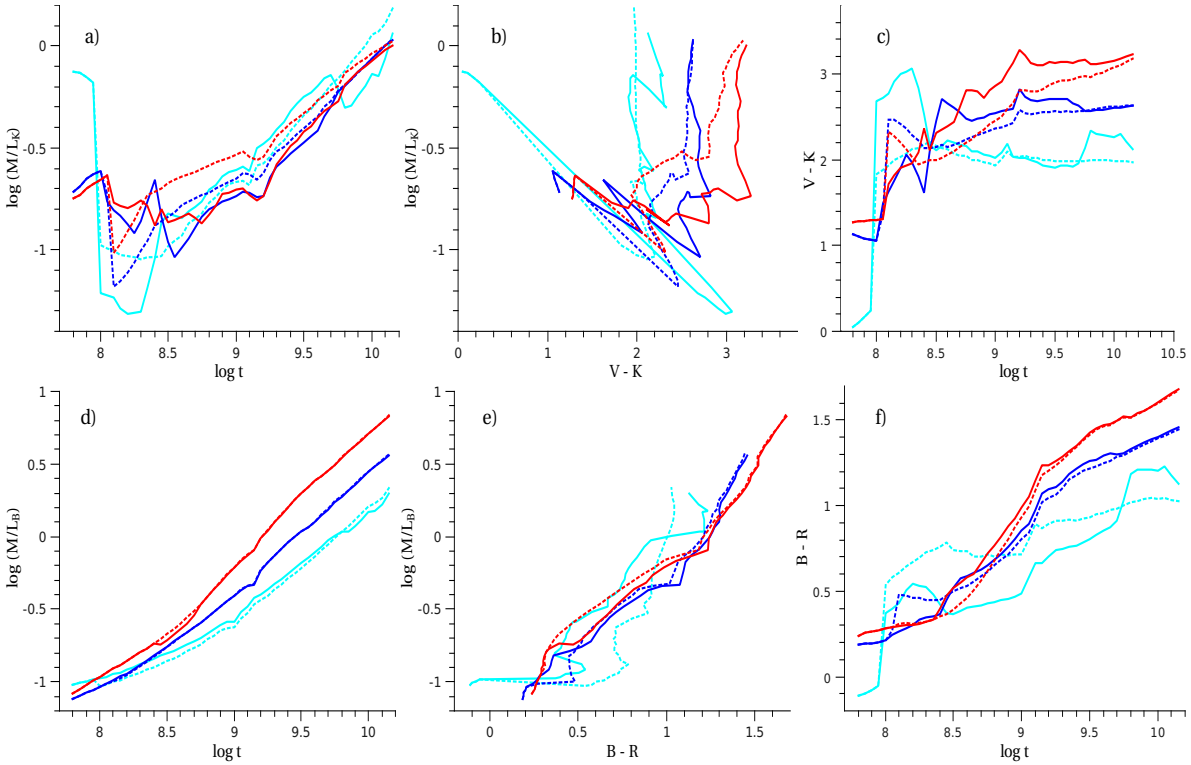

Figure 9: Comparison of SSP properties between 2002 and 2009 data sets. Continuous lines represent the 2009 data set, dotted lines 2002 set. Three metallicities with Z=0.0001 (cyan lines), 0.004 (blue lines) and 0.019 (red lines) are presented. See text for details.

(SMC) and solar neighborhood. We show separately the time evolution of colors and M/L in the left and right panels respectively and in the middle panels the color - M/L relations. The lower row shows the results in B band, upper in K band. Looking at panel c, we can see the time evolution of $V-K$ color for our SSP models. The AGB phase transition occurs at slightly different times, depending on the metallicity. Roughly, the onset of AGB occurs around 10^8 yr. The phase transition effect can be seen clearly in $V-K$ with a jump of nearly three magnitudes towards K for the low-Z 2009 model. With higher metallicities, a sudden change in color does take place, but in a lesser magnitude. There is an apparent difference in the behavior of the 2002 and 2009 models. The old models exhibit a sharper jump to the red for the two higher metallicities, shown as blue and red dotted lines in the figure. For the new models (solid lines), the transition to the red starts with a small jump at the onset of AGB and

then develops over a prolonged period of time resulting in a total change of color comparable to that of the old model. The reason behind this lies in the treatment of the hot-bottom burning (HBB) in the new models.

For an AGB star in the HBB mass range, HBB causes an increase in the luminosity of the star. The higher luminosity leads to a higher mass-loss rate and when the envelope has lost enough mass, the HBB ceases and the star goes down in luminosity. The star then settles on an evolutionary behavior corresponding to a star born with a lower initial mass. The over-luminosity effects gets weaker with decreasing stellar mass - the stars spend less time in the over-luminous phase and enter normal evolutionary behavior with a less diminished envelope. This process causes temporal widening of the AGB phase transition color jump, as seen in the $V-K$ color and also in the M/L ratio (panel *a*) in Figure 9. The difference between old and new models is reversed in the low-Z models. In this case the change in $V-K$ is greater in the new model than in the old one. This can be explained by the occurrence of the third dredge-up, which in the refined models allows for an early formation of carbon stars (see section 2.2).

In the optical regime, the color change is less significant. Looking at panel *f*, we can see that in the solar metallicity models, the is no transition towards red in either the new or the old models at the onset of AGB. This is quite expected as the MS and core He-burning (CHeB) phases dominate the optical colors. Still, in the low-Z models, a jump to the red can be seen in the $B-R$ color. This is because the stars with lower metallicities develop the AGB phase at higher effective temperatures, causing a transition also in the optical colors of the population at the onset of the AGB phase.

A prominent spike can be seen in the new K-band models at metallicity $Z = 0.004$. Looking at panel *a*, we can see that at SSP age $\log(t/\mathrm{yr}) = 8.25$, the mass-to-light ratio takes a sudden turn to higher values, and in panel *c* the $V-K$ color shows a corresponding shift to the blue. As the K band luminosity is very sensitive to the contribution from carbon stars, the feature in mass-to-light of the SSP can be ascribed to the non-smooth onset of the C star phase as a function of stellar mass for this particular metallicity, shown in Figure 10. The thin lines represent the O-rich configurations (M stars) and the thick lines mark the C-rich configurations (C stars). At very low metallicities virtually all AGB stars develop an extended C star phase at the end of their evolution and at solar metallicity, stars in the mass range of roughly 2–4 $\mathrm{M}_\odot$ do. At $Z = 0.004$ though, the onset and length of the C star phase is very

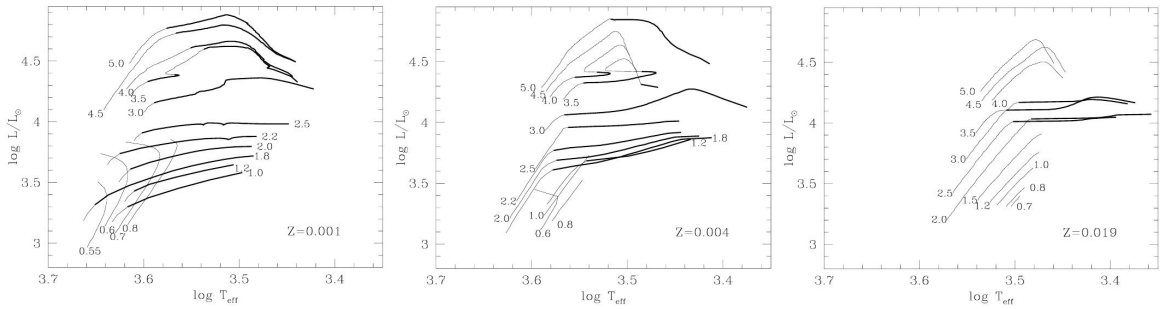

Figure 10: TP-AGB tracks in the HR diagram for three metallicities and a range of initial masses. Luminosity and effective temperature corresponds to the quiescent values before thermal pulses. Surface O-rich and C-rich configurations are marked with thin and thick lines respectively. (Marigo and Girardi, A&A, 469, 239, 2007, reproduced with permission © ESO.)

mass-dependent between 3 and 5 $M_\odot$, with C and M star phases alternating along some stellar tracks. This behavior results from a complex interplay of third dredge-up and mass loss, that tend to favor the formation of C stars, and HBB, that tends to inhibit it, and their dependence on mass and metallicity; see the original paper by Marigo and Girardi (2007) for details. At ages $\log(t/\mathrm{yr}) = 8.25 - 8.4$, the brightest stars in the $Z = 0.004$ SSP are between $3.5 - 4.5$ $M_\odot$, which lack the extended C star phase; this causes the sudden drop in the K band luminosity with respect to slightly younger and older ages.

As discussed already in section 2.2, the new models produce an excess of AGB luminosity at ages $\log(t/\mathrm{yr}) \geq 9.7$ for the three lowest metallicities included in this work. The effects of this excess luminosity output can be seen both in $V - K$ and $B - R$ colors (panels c and f). The $Z = 0.0001$ models experience a jump towards red at this point. The impact to the B band M/L value is very small and can barely be seen in panel d, whereas the impact in the K band is quite distinct. Once again it should be noted that the "incorrect" evolution is a result of limitations in the low-Z AGB models. Ignoring the late age AGB over-luminosity, the new models at the lowest metallicity should rather follow a path more parallel to the old models.

2.4.2 Effects of the RGB phase

The onset of the red giant branch at around 1 Gyr ($M_{\mathrm{TO}} \sim M_{\mathrm{HeF}}$) does not exhibit a shift in the integrated colors as does the AGB phase. Some authors have argued that a RGB phase transition should occur because of a supposed increase in fuel consumption in stars with $M \lesssim M_{\mathrm{HeF}}$,

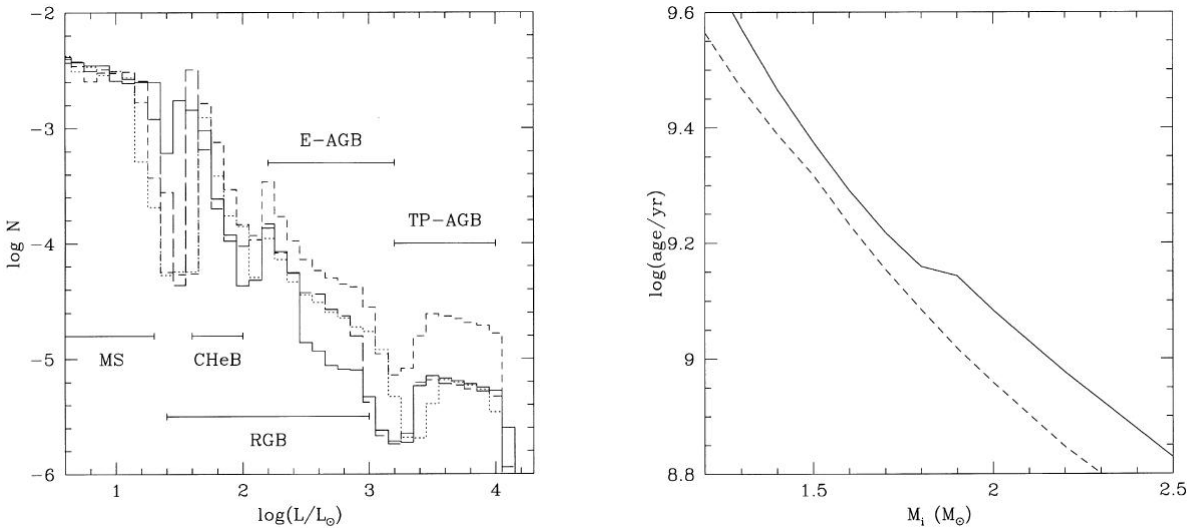

Figure 11: *Left panel:* The luminosity functions for four isochrones with $Z = 0.008$. The ages of the isochrones are $\log(t/\mathrm{yr}) = 9.05$, 9.10, 9.15 and 9.20 (continuous, long-dashed, short-dashed and dotted lines respectively). The age interval spans from the development of the RGB to the end of the red phase. The increase in number of AGB stars present in the $\log(t/\mathrm{yr}) = 9.15$ isochrone is significant. *Right panel:* The lifetimes of the $Z = 0.008$ stellar tracks up to the end of the main sequence, t_{H} (dashed line), and up to the end of the CHeB, t_{eHe} (continuous line). From Girardi and Bertelli (1998).

due to a significant increase in the core mass during the RGB phase. In a stellar population, no net increase in the fuel consumption takes place, rather a rearrangement of fuel consumed in different evolutionary phases (Girardi and Bertelli, 1998). The increase in RGB fuel consumption (and an increase in luminosity) is counteracted by a decrease in AGB and CHeB fuel consumption. That is, a certain amount of fuel burned on the CHeB and AGB phases in stars with $M > M_{\mathrm{HeF}}$ is burned during the RGB phase in stars with $M < M_{\mathrm{HeF}}$. The rearrangement of fuel burned occurs mainly from CHeB and E-AGB phases to the RGB phase. As RGB and E-AGB stars have very similar spectral energy distributions, no changes in the integrated colors due to RGB phase transition can be seen.

After the RGB transition though, a spike to the red can be seen in the integrated colors at $\log t \simeq 9.1 - 9.2$. This causes even a noticeable dip in the M/L curves. Due to its clearly transient nature, this phenomenon is not to be associated with the RGB phase transition discussed above as it does not cause a permanent jump to the red. The left panel of Figure 11 shows the

luminosity functions for four isochrones from the Padova library (at the resolution of 1998) with $Z = 0.008$ and ages $\log(t/\mathrm{yr})$ ranging from 9.05 to 9.20. The $\log(t/\mathrm{yr}) = 9.15$ isochrone shows a large increase in the number of AGB stars. This temporary excess is the origin of the red spike feature in the models. But what causes this excess in the first place?

The birth rate of AGB stars can be expressed as

$$b^{\mathrm{AGB}}(t) = \Phi_{M_{\mathrm{eHe}}} \left| \frac{\mathrm{d}t_{\mathrm{eHe}}}{\mathrm{d}M_{\mathrm{i}}} \right|^{-1}_{M_{\mathrm{i}}=M_{\mathrm{eHe}}} \simeq \Phi_{M_{\mathrm{TO}}} \left| \frac{\mathrm{d}t_{\mathrm{eHe}}}{\mathrm{d}M_{\mathrm{i}}} \right|^{-1}_{M_{\mathrm{i}}=M_{\mathrm{TO}}}, \quad (3)$$

where the subscript 'eHe' refers to the quantities evaluated at the end of the CHeB phase and the subscript 'TO' refers to the quantities evaluated at the main sequence turn-off. The birth rate $b(t)$, or the evolutionary flux, gives the number of stars which leave the CHeB phase (or the MS) by unit time. The right panel of Figure 11 shows the functions $t_{\mathrm{H}}(M_{\mathrm{i}})$ (the main sequence lifetime) and $t_{\mathrm{eHe}}(M_{\mathrm{i}})$ (the lifetime up to the end of the CHeB) for the $Z = 0.008$ evolutionary tracks over a range of ages and masses in the vicinity of the observed red bump feature. We note that t_{H} is a quite smooth, decreasing function of mass, but t_{eHe} displays a flattened feature at an age of $\log(t/\mathrm{yr}) = 9.15$. The flattening of t_{eHe} occurs because the He-burning lifetime is shortened by a factor of about 2 after the RGB develops. According to equation 3, this flattening causes an increase in $b^{\mathrm{AGB}}(t)$, meaning an increase in the number of AGB stars formed at this age. This results in the jump to the red in the integrated colors. The age at which the red bump appears does not coincide with the onset of the RGB, but is delayed by about 1×10^8 yr. The delay corresponds to the time lag between ages in which the stars with $M = M_{\mathrm{HeF}}$ are either RGB or AGB stars. The time lag is comparable to the He-burning lifetime, about 1.5×10^8 yr.

This temporary jump to the red would be very hard to confirm with observations due to its short lifetime. The magnitude of the shift towards red is quite small and may be severely affected by observational uncertainties. Furthermore, if the uncertainties can be reduced, the intrinsic properties of the observed population must be strictly constrained. First, the stars of the population should be coeval to within 10^8 yr in order to prevent temporal spread in the colors. This can hardly be achieved with any sizeable population. Secondly, the metallicity spread of the population should be small enough. Since the red bump occurs at different

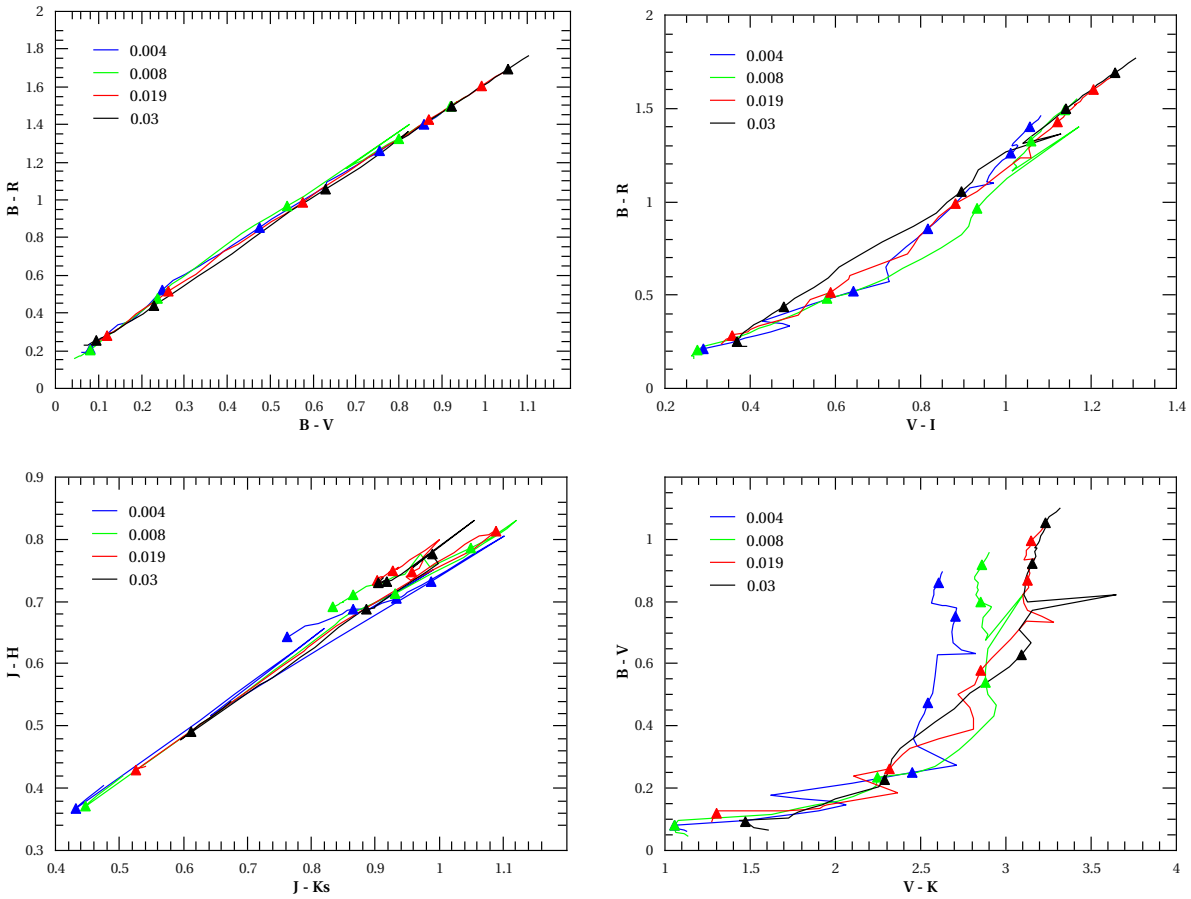

Figure 12: Two-color diagrams for the 2009 dataset with four metallicities shown on the panels. The triangles indicate SSP ages $\log(t/\mathrm{yr}) = 8.0$, 8.5, 9.0, 9.5 and 10.0. See the text for details.

times for different metallicities, a substantial spread in initial metallicity distribution would again cause temporal spread in the colors. In Section 3 we will see that in composite stellar populations the red bump feature gets completely smoothed out.

2.4.3 Color-color correlation

In Figure 12 we can see a set of color-color diagrams plotted for the 2009 SSP with four metallicities ($Z = 0.004$, 0.008, 0.019 and 0.03). The model ages range from $\log(t/\mathrm{yr}) = 7.8$ to 10.15. The triangles indicate SSP ages $\log(t/\mathrm{yr}) = 8.0$, 8.5, 9.0, 9.5 and 10.0. The lowest ages are located in the lower left corner of the plot with increasing ages towards redder colors.

The top left panel shows $B-R$ color plotted against $B-V$. We can see that there is a clear linear correlation between the colors with all metallicities sharing virtually the same track. In the blue part of the plot, the age of the model more or less determines the colors, while in the red, the governing quantity is metallicity. The spread in colors with varying metallicity is relatively small for the lowest two ages indicated. Therefore, the colors of the population can be used to give a rough estimate of its age even if the metallicity is unknown. With redder colors and thus higher ages, the increasing spread between metallicities makes this evaluation unfeasible, unless metallicity is known.

In the top right panel, we can still see some correlation between $B-R$ and $V-I$ colors, but with greater spread than in the case of $(B-R, B-V)$. The age-metallicity degeneracy is less tight towards redder colors such as $V-I$. In the lower left panel, a two-color plot with near-infrared 2MASS colors $(J-H, J-K_s)$ is presented. In this plot, the possible values in the two-color plane are quite restricted, with most of the SSP colors occupying an area in the top right corner of the plot with only the youngest SSP ages in the lower left part of the plot. Neither metallicity nor age have much effect on the evolution of colors in this case. The last panel in the lower right corner presents a plot with $B-V$ vs. $V-K$. The behavior of the colors is far from linear. $V-K$ saturates at ages $\gtrsim 1$ Gyr, from which on the $V-K$ color is almost constant throughout the rest of the evolution, while $B-V$ evolves to the red over time. At old SSP ages, $V-K$ appears to be a fairly good metallicity indicator, at least up to the solar metallicity (seen also in Figure 9, panel *b*). The $Z = 0.019$ and 0.03 models both saturate at equal $V-K$ levels and cannot be distinguished from each other.

As a conclusion, the color-color relations are affected by the age-metallicity degeneracy which is very tight in the optical-optical and can be partially lifted when combining optical and near-infrared colors.

2.4.4 Mass-to-light–color correlation

The stellar mass-to-light ratio is an important quantity in astrophysics as it allows translation between photometry and dynamics by recovering the underlying stellar mass from the observed luminosity. For example, the stellar M/L ratio is needed for the spiral galaxy rotation curve decompositions. The determination of correct mass-to-light values is crucial in order to determine the dark matter contribution to a rotation curve of a galaxy. In order to find out the

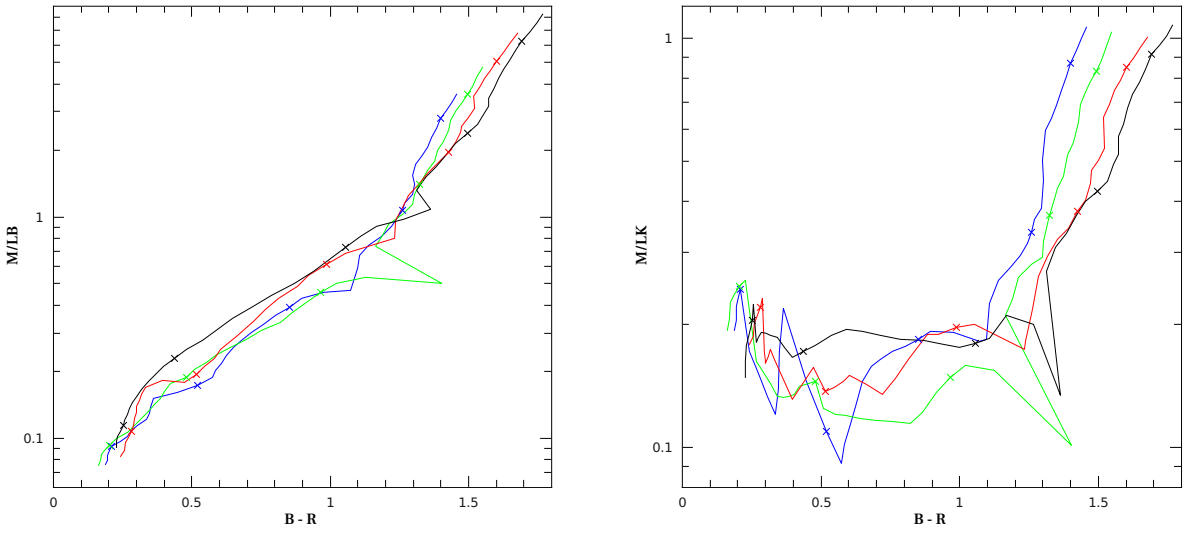

Figure 13: Mass-to-light–color correlations for 2009 models at four metallicities: Z=0.004, 0.008, 0.019 and 0.03 (blue, green, red and black lines respectively). The crosses mark SSP ages $\log(t/\mathrm{yr})$ = 8, 8.5, 9, 9.5 and 10, with highest ages at the top of the figure. *Left panel:* B band mass-to-light vs. $B-R$ color *Right panel:* K band mass-to-light vs. $B-R$ color.

M/L ratio for a stellar population, the ratio has to be connected to some observable. Stellar population synthesis models have shown that there is a correlation between stellar mass-to-light ratios and broadband colors (Bell and de Jong, 2001).

In Figure 13 there are B and K band mass-to-light ratios plotted against $B-R$ color for the 2009 dataset. We can see on the left panel that the relation between the logarithm of mass-to-light ratio in the B band and the $B-R$ color is almost linear and displays a fairly tight age-metallicity degeneracy. This kind of correlation also holds for other optical-optical relations. The distinct spike in the $Z = 0.008$ model is the red bump discussed in section 2.4.2. Apart from this spike, the M/L ratio evolves quite smoothly as a function of color.

The correlation is not as clean when inspecting the K band M/L ratio against $B-R$ color (right panel). Before the red bump age, the changes in the M/L ratio are erratic and quite large. After the bump though, and thus for the most of the SSP lifetime, the behavior of the relation is quite smooth. Unfortunately, there is a significant spread in the colors as a function of metallicity. This makes the correlation quite less tight for the well-behaving, older age part of the relation. So, although the near-infrared bands are often considered to be the best mass

tracers as these bands are less sensitive to interstellar dust effects and recent bursts of star formation than the optical bands, the color corrections from luminosities to masses are less robust due to their metallicity dependence.

Even though the optical-optical relation does not reach a complete metallicity degeneracy, optical colors provide a good means to derive the mass-to-light ratio of an SSP. But the real interest in the correlation arises when one examines more complex populations that can be used to model a wider range of real world objects, like galaxies. The M/L-color correlation will be next derived for models with varying star formation histories.

3 Models with varying star formation rates

3.1 From SSPs to more complex models

The results derived from SSP models only apply to a very limited range of real populations, such as star clusters. The possible populations are constrained by SSP model requirements for coeval and chemically homogeneous stars. But most of the objects of astrophysical interest are not this simple. The stellar ages of a real population differ due to star formation in the course of the evolutionary history of the population. In addition, the chemical enrichment of the interstellar medium (ISM) by previous generations of stars cause a gradual increase in the metallicity of the future generations. Furthermore, to accurately model a complex population like a spiral galaxy, one has to take into account several other factors. One of such factors is how the galaxy interacts with intergalactic medium. In open models, there is a certain amount of gas falling into the galaxy and escaping it due to galactic winds. Naturally, in closed models, no exchange of gas occurs with the surroundings. In describing the mixing of metal-enriched gas into the ISM, one has to introduce some sort of galactic dynamics into the model. Also one has to address the differences in characterizing the evolution of the bulge and the disk and the varying evolution of disk populations as a function of radial distance in the disk. In this work, while one is aiming to provide results applicable to galaxies, this level of detail is not pursued. We move on from SSPs towards more complex populations by introducing variable star formation rates (SFR) and constant metallicity. This kind of models are commonly used in the literature and we shall see that this level of detail is sufficient to describe a range of stellar populations and to improve upon some results presented in the literature, especially the ones related to the mass-to-light–color correlation and the impact of proper modeling of the AGB phase on it.

3.2 Simple exponential models

Simple stellar populations form the basis of the variable SFR models. The SSP luminosity (L^{SSP}, equation 1) is convolved with the star formation history (SFH) $\Psi(t)$ to get the luminosity of a system of age T in any given band:

$$L = \int_0^T \Psi(t) L^{\mathrm{SSP}}(T - t) dt, \tag{4}$$

where $T - t$ is the age of an SSP born at time t. We shall use one of the simplest of models for the varying star formation history, an exponentially decaying (or increasing) star formation rate. This SFH can be expressed as

$$\Psi(t) \propto e^{-t/\tau},$$

where τ is the e-folding timescale of the star formation rate. The age of the system is 10 Gyr in our models, corresponding to the age estimated for the bulk of the stellar population in the Milky Way disk (Carraro, 2000). The timescales τ of exponentially declining star formation rates range from 1.55 [Gyr] to ∞ (constant SFR). For the exponentially increasing SF rates, negative values of τ have been used.

In addition to the e-folding timescale parameter τ, the star formation history can be quantified with a birth rate parameter b (Scalo, 1986):

$$b = \frac{\psi(T)}{\langle\psi\rangle} \qquad\qquad \langle\psi\rangle = \frac{1}{T}\int_0^T \psi(t)dt, \tag{5}$$

where $\psi(t)$ is the SFR at time t. The b parameter gives the ratio between the present and past average star formation rates. The b parameter is also used as a morphological indicator between different Hubble types for spiral galaxies. Kennicutt, Tamblyn and Congdon (1994) showed that the change in the photometric properties of spiral galaxies along the Hubble sequence is mainly due to changes in the star formation histories of disks, and only secondarily to changes in the bulge-to-disk ratio, which had been previously used as a primary morphological indicator. According to their classification, the b parameter increases with later Hubble type, so that $b < 0.2$ for Sa–Sab disks, $b \sim 0.3 - 0.4$ for Sb disks and $b \sim 0.8 - 1$ for Sbc–Sc disks. The relation breaks down with larger values of the b parameter because the later Hubble types display rather irregular star formation histories. Thus, constructing composite stellar population models with different b parameters (with $b \lesssim 1$) roughly represents spiral galaxies of different Hubble types. The models with $b > 1$ represent blue galaxies with recent episodes of star formation. The larger the b parameter value, the younger the system is on average. With varying star formation histories, we are able to model quite a broad range of galaxies with different morphologies. In addition, elliptical galaxies are often rather well represented by old SSPs.

The b parameter values used in this work, corresponding to the range of τ values, range from 0.01 to 10.0, with $b = 1.00$ naturally corresponding to constant star formation rate. The

b	0.01	0.05	0.10	0.15	0.20	0.30	0.40	0.50	0.60	0.70	0.80	0.90	1.00	
	1.10	1.23	1.37	1.55	1.75	2.01	2.35	2.84	3.23	3.67	4.59	6.46	8.33	10.00
τ	1.55	2.20	2.80	3.25	3.80	4.90	6.20	8.00	10.50	15.00	23.00	50.00	∞	
	-50.00	-23.00	-15.00	-10.50	-8.00	-6.20	-4.90	-3.80	-3.25	-2.80	-2.20	-1.55	-1.20	-1.00

Table 3: The b parameter values and the corresponding τ values.

full range of b and corresponding τ values are tabulated in Table 3.

3.3 2009 versus 2002

The results for exponential star formation histories will be presented using mostly the 2009 dataset. Before we move on to examine the results in detail, we shall briefly examine the differences between the old and new models.

In Figure 14 we find the mass-to-light plotted against b parameter values and colors for our 10 Gyr model. The 2002 and 2009 models are drawn with dashed and solid lines, respectively. Earlier, as we compared the old and the new SSPs, we saw that in the optical bands, there is little difference between the quantities of the SSPs. Naturally, this is also the case with the exponential SFH models. In the I band (top right panel) we begin to see some difference between the old and the new models. In the K band, the difference is clearly noticeable. The $b = 0.01$ case is the closest one to an SSP with most of the star formation occurring during the early ages of the population. Looking back at panel a in Figure 9 we can see that the 2002 and the 2009 SSPs are really close to each other when 10 Gyr old. The difference between the SSPs gets larger at lower ages. As a consequence, the old and the new K band exponential models start with M/L values very close to each other. The same applies to the I band. As we move towards higher b parameter values and more recent star formation, the difference between the models gets bigger. In the K band, the difference at $b = 1.0$ (better seen in Figure 15) is about 0.1 dex and it stays around that level to the higher b values. In the I band, the difference at $b = 1.0$ is very small for $Z = 0.004$ and the difference remains very small all the way to the highest b values. For the two other metallicities the difference between the old and the new models at both $b = 1.0$ and $b = 10.0$ is about 0.05 dex.

In the lower panels of the figure we find the M/L plotted against $V - K$ and $B - R$ colors. As expected, the new models result in redder colors than the old ones. In the lower left panel

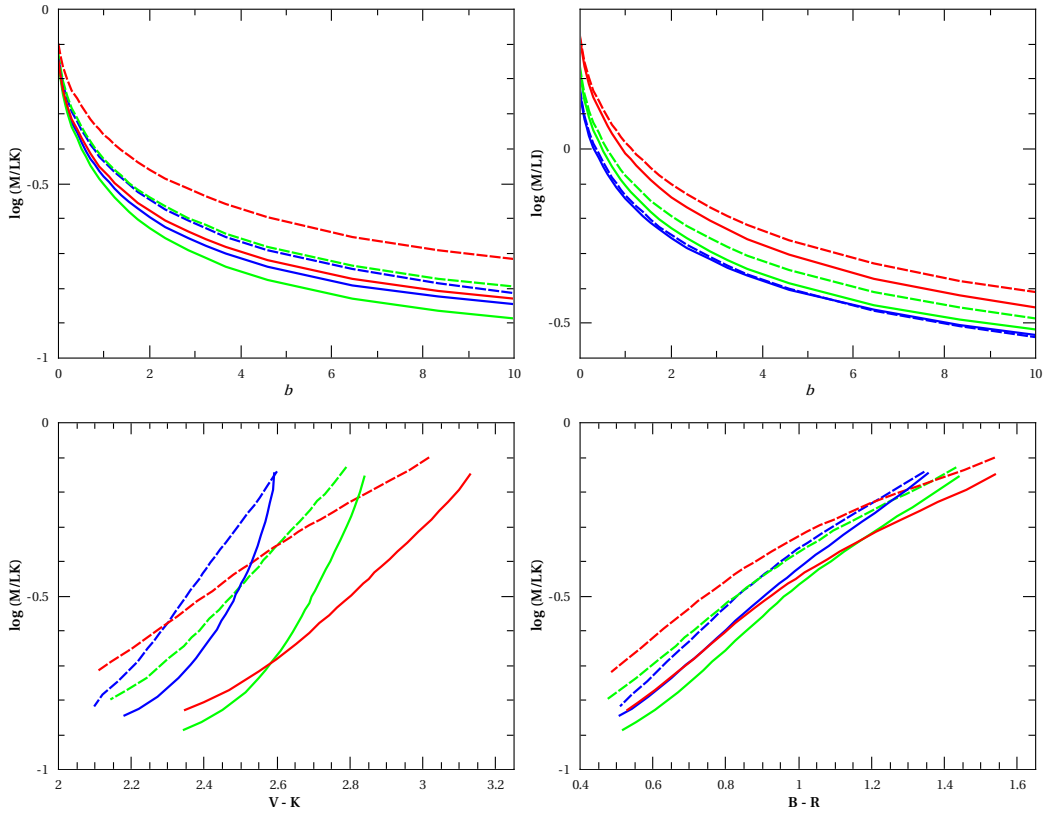

Figure 14: *Upper panels:* Mass-to-light values as a function of the b parameter for three metallicities. Left panel shows the M/L in K band, right panel in I band. *Lower panels:* K band mass-to-light versus $V-K$ (left) and $B-R$ (right) for three metallicities. Solid lines represent the 2009 values and dashed lines the 2002 values.

we can see that the $V-K$ color difference gets even more distinct with increasing metallicity. In the lower right panel we find that the M/L_K decreases with negligible shift of $B-R$. It is good to notice that the level of degeneracy in $V-K$ color is greater in the old models than in the new ones. This is also true for other optical–near-IR color combinations. Thus the improved AGB models produce slightly less tight MLC relations with these colors.

Looking at the top left panel of Figure 14 or the left panel of Figure 15, we can see that the behavior as a function of metallicity in the 2009 models is not monotonic. The $Z = 0.008$ set is brighter in the K band than both the 0.004 and the 0.019 sets. This kind of non-monotonic behavior results from the more detailed treatment of the TP-AGB phase and can be seen also

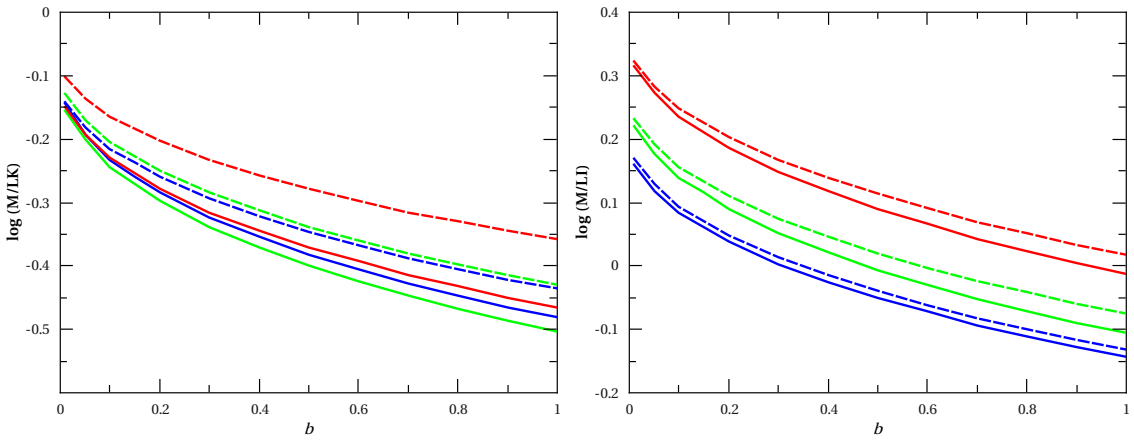

Figure 15: Mass-to-light values as a function of the b parameter, zooming into $b \leq 1$. Left panel shows the M/L in K band, right panel in I band. Solid lines represent the 2009 values and dashed lines the 2002 values.

in SSPs when all the metallicities are plotted together.

We conclude that the results are as expected based on the results from SSP models; the new models are more luminous in the near-infrared bands than the old models leading to somewhat lower near-IR M/L values and redder colors.

3.4 Johnson-Cousins bands

In Figure 16 we show the B and K band mass-to-light plotted against $B-R$ and $I-K$ colors for the exponential SFH models based on the 2009 SSPs. A number of models with different metallicities and b parameter values are combined to show trends in the exponential models. The solid color lines connect models with the same metallicity and the dashed lines connect models sharing a common b parameter. The b parameter values shown on the plot are 0.01, 0.15, 0.40, 0.70, 1.00, 1.75, 3.67 and 10.00 - from top to bottom. The thick dotted line is a pure 10 Gyr old SSP drawn in for the sake of extending the color and age range to values typical of old elliptical galaxies. We notice that the M/L ratio for the model with the smallest b parameter value smoothly extends to the pure SSP ratio.

The top left panel shows $\log(M/L)$ at B band as a function of $B-R$ color. We can see that there is a tight correlation between the M/L ratio and the optical colors that is very little

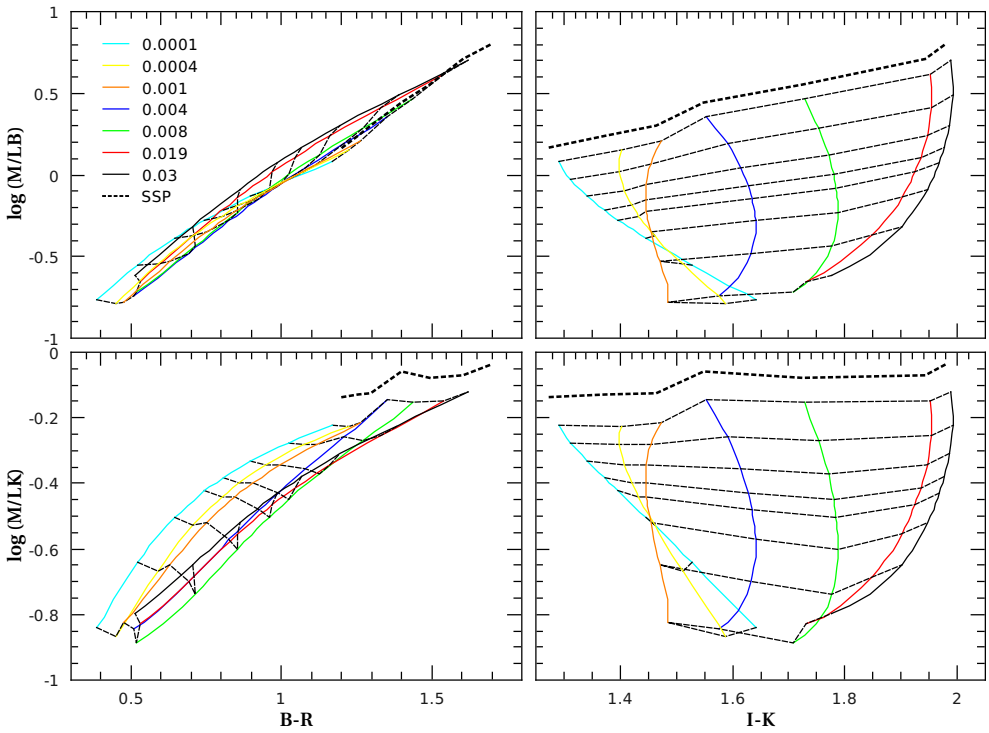

Figure 16: Mass-to-light–color correlations combining M/L at B and K bands against $B-R$ and $I-K$ colors for a range of b values and metallicities. The colored solid lines connect models with the same metallicity and the dashed lines connect models with the same b parameter. The dashed lines are drawn for following subset of b values (from top to bottom): 0.01, 0.15, 0.40, 0.70, 1.00, 1.75, 3.67, 10.00. The thick dotted line represents a pure SSP of age 10 Gyr. Metallicities are listed on the top left panel.

affected by metallicity and SFH. The varying star formation rates have no effect on the age-metallicity degeneracy inherited from the SSPs. This provides us with good grounds for solid mass-to-light–color relations (or MLC relations in short). The situation is quite good even in the K band M/L versus $B-R$. Here the age-metallicity degeneracy is not as tight, but still a fairly solid relation can be established, especially if we neglect the three lowest metallicities: $Z = 0.0001$, 0.0004 and 0.001. There are good reasons to disregard these metallicities. First, as already noted briefly in Section 2.2, a real 10 Gyr old galaxy is seldom this metal poor due to internal chemical enrichment. As noted by Bell and de Jong (2001), chemical evolution caused by even modest amounts of star formation raises the galaxy metallicity rapidly to at least 0.1 solar ($Z = 0.002$) even in a closed box case. Secondly, neglecting the three lowest

metallicities relieves us from slight errors caused by the extra AGB luminosity occurring at SSP ages around 5 Gyr, even though the errors are smaller than in the SSP case due to extended star formation histories. Taking these metallicities out of the picture, the metallicity spread becomes a lot narrower.

In the $I-K$ colors (right hand side panels) the age-metallicity degeneracy breaks down. The star formation history more or less determines the M/L ratio while color is mainly determined by metallicity, especially in the low-b cases. The picture becomes more complicated with increasing b parameter values. $I-K$ is sensitive to red giant phases which shows in the low-Z models as the order of metallicities as a function of color is reversed. This is due to more massive AGB stars entering the carbon phase and causing the greater color transition towards the red, the lower the metallicity. However. if we exclude these three lowest metallicities for the reasons argued above, the trend of $I-K$ as a function of metallicity is rather monotonic. Since $I-K$ is basically a metallicity tracer, quite independent of the age and M/L ratio of the underlying population, defining MLC relations in $I-K$ is quite meaningless.

3.4.1 Model comparison

To highlight the importance of the improved treatment of the TP-AGB phase on MLC relations, we now compare the results of our exponential SFH models to the ones presented in Figure 2 of Bell and de Jong (2001), hereafter BdJ. This figure is reproduced in our Figure 17. The BdJ results were based on the population synthesis models of Bruzual and Charlot (2003) that, like other public population synthesis models from those years, did not include a detailed account of the AGB phase (while this has been improved in more recent releases: Bruzual 2007). Like ours, the BdJ models are calculated for a single-metallicity exponentially declining star formation history. The M/L ratios for Salpeter IMF in B band (panels a and b) and K band (panels c and d) are shown against the model $B-R$ (panels a and c) and $I-K$ (panels b and d) broadband colors. Models of the same e-folding timescale τ are connected with solid lines and models of the same metallicity are connected by dashed lines.

The bands and colors are the same as in our Figure 16. There are some differences that need to be accounted for. BdJ use a Salpeter IMF, which causes an increase in M/L of about 0.15 dex with respect to our model. An additional 0.1 – 0.15 dex increase comes from the older age of the BdJ model, 12 Gyr. The total offset in M/L is about 0.3 dex in B band. One

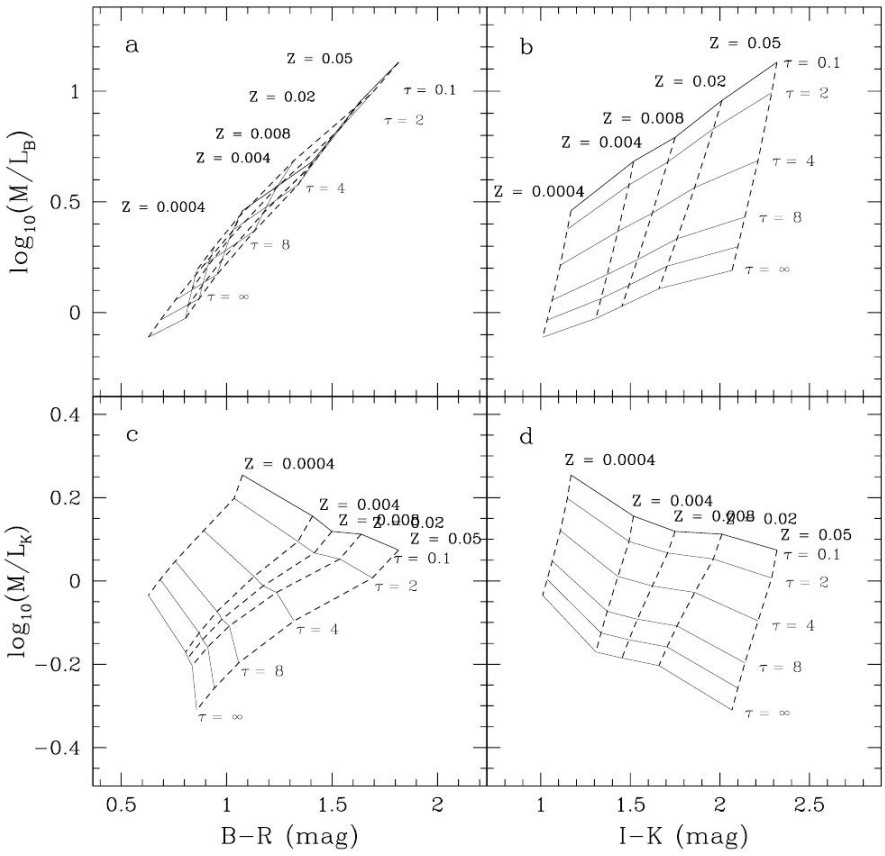

Figure 17: Trends in exponential SFH model stellar M/L ratios with color from Bell and de Jong (2001). See text for details. Reproduced by permission of the AAS.

should also note that the ranges of the parameters (metallicity and SFR e-folding timescale) are slightly different. BdJ model metallicity goes up to $Z = 0.05$, but is missing our lowest metallicities. In the lower end of the SFR e-folding timescales BdJ start with a very small value of $\tau = 0.1$, which is close to an SSP. The second solid line ($\tau = 2$) in the BdJ model is actually a quite close match to our $b = 0.01$ ($\tau = 1.55$) line. The highest value of τ in BdJ models correspond to a constant SFR, which is the fifth dashed line in our Figure 16. To make the comparison easier, we re-plot our figure with a limited set of b-values up to 1.00, matching the maximum τ value in BdJ. The resulting plot is presented in Figure 18.

Keeping in mind the corrections presented above, the values in B band M/L seem to be fairly consistent between our models and the BdJ models. Both cases exhibit an increasing

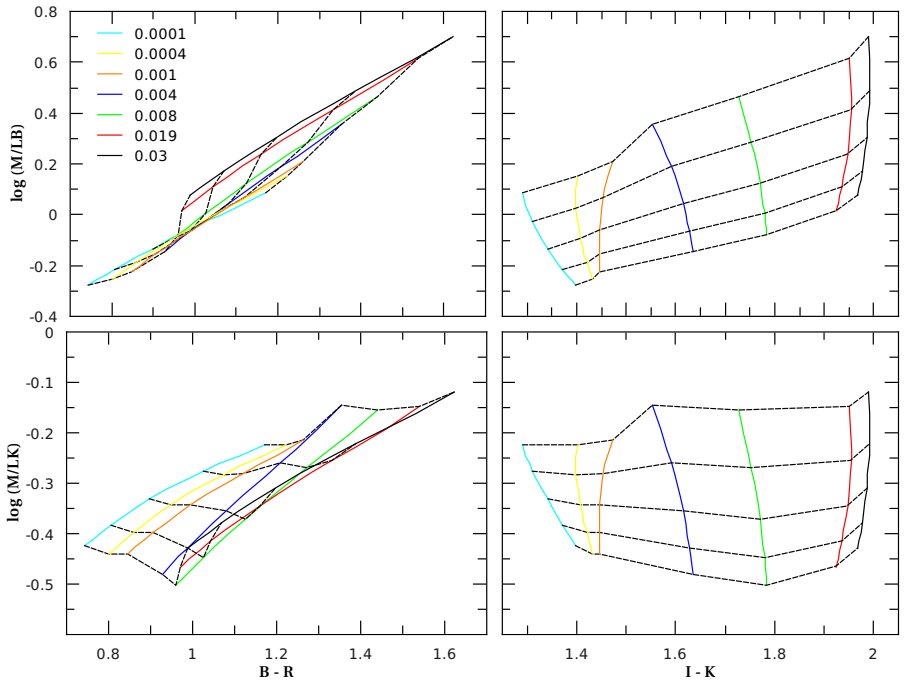

Figure 18: The same as Figure 16, but with b parameter values only up to 1.00 and SSP not shown.

trend in M/L with increasing metallicity, as seen clearly in the top left panels of both plots. The color spread in $I-K$ is somewhat narrower in our models, and there are slight differences in the trends seen in the top right panels. The colors of a specific metallicity in BdJ tend to the blue with increasing τ, while in our models the trend is the opposite for the intermediate metallicities or stagnant for the highest metallicities. In the K band though, the plots look quite different from each other. The BdJ models show a decreasing trend with increasing metallicity both in $B-R$ and $I-K$, while our models result in roughly metallicity independent M/L values compared to BdJ. In $B-R$ our models present a greater degree of metallicity degeneracy than the BdJ models, especially when neglecting the three lowest metallicities. This allows for quite robust K band MLC relations at $B-R$. The same applies to K band M/L versus optical colors in general.

The reason for the different behavior is unveiled by inspecting Figure 19. This figure is the same as Figure 18, but excluding the TP-AGB phase from our models. We can see that the changes in all MLC relations involving K band are dramatic. The new plots seem almost

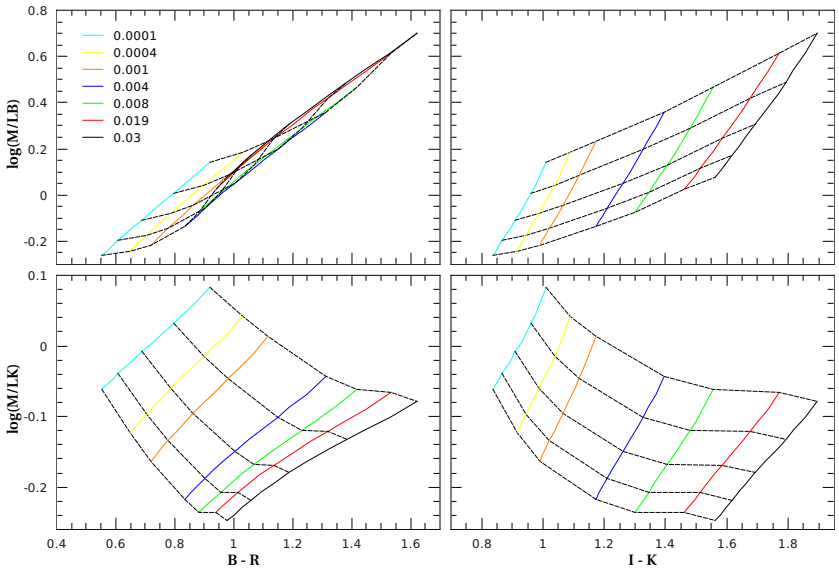

Figure 19: The same as Figure 18, but with TP-AGB excluded from the models.

identical to the BdJ ones. Dropping the TP-AGB phase obviously causes a loss in K band luminosity and results in higher M/L ratios than in the previous figure. The colors are also affected. The spread in $B-R$ and especially in $I-K$ becomes larger, providing an excellent match to the BdJ colors. The decreasing trend with increasing metallicity is also produced in the new plots. The degeneracy effect seen in the lower left panel of Figure 18 is far less tight now, corresponding well to the models presented by BdJ. The only plot that is left relatively unchanged is the top left panel showing a combination of optical-optical quantities that are quite unaffected by the AGB phase.

This is an outstanding example of the importance of the AGB phase in the stellar population synthesis models and in MLC relations in particular. Unless relying only on the bluest bands, the AGB phase should not be neglected when constructing these models, especially if near-IR bands are used, as is most often the case for stellar mass estimates.

3.4.2 Mass-to-light–color relation fits

The main goal of this work is to provide updated MLC correlations with TP-AGB phase being accounted for at the level of 2009. We now present the M/L-color relations resulting from

Color	s_B	z_B	s_V	z_V	s_I	z_I	s_K	z_K
$B-V$	1.87	−1.08	1.47	−0.81	1.15	−0.70	1.06	−1.07
$B-R$	1.27	−1.29	1.00	−0.98	0.78	−0.84	0.72	−1.19
$B-I$	1.04	−1.55	0.82	−1.18	0.64	−1.00	0.59	−1.33
$V-I$	2.31	−2.11	1.83	−1.63	1.43	−1.35	1.30	−1.64
$V-K$	1.28	−3.50	1.04	−2.80	0.83	−2.31	0.64	−2.20

Table 4: Coefficients for the linear fits to MLC relations for our exponential SFH models with Kroupa98 IMF. The slope s and zero point z are tabulated for different bands and broadband colors.

our simple exponential models using the Kroupa98 IMF. The relations have been constructed by implementing least-squares linear fits to our model points for the four metallicities with $Z \geq 0.004$. The resulting relations are in the form $\log(M/L) = s_i \times (color) + z_i$, where s is the slope and z is the zero point for the relation in band i. The coefficients are tabulated in Table 4.

In the bluer bands the relations are in very good agreement with the results presented in Table 1 of BdJ, where they assume a mass-dependent formation epoch with bursts model and adopt a scaled-down Salpeter IMF. The scaled down IMF is equivalent to a normal Salpeter IMF with a flat $x = 0$ slope below 0.35 $M_\odot$. The agreement between BdJ and our results holds in B, V and I bands and up to $V-I$ in color. Our models produce slightly higher values but the differences in slope are very small. The zero points are also very similar, due to a very small zero point correction between the Kroupa98 and the scaled-down Salpeter IMFs. In the K band and $V-K$ color our relations have significantly steeper slopes than those presented in BdJ. Again, the difference arises from the modeling of the AGB phase.

Portinari et al. (2004) also provided MLC relations for their 10 Gyr old disk galaxy models using a set of IMFs, including the Kroupa (1998) IMF. In general, the slopes given in their Table B1 are somewhat shallower than ours or the the ones by BdJ, with the exception of slopes involving K band M/L or colors. In these cases, the slopes are steeper compared to BdJ results, but still shallower compared to our results. The slightly better agreement with our results in the near-IR is due to simple TP-AGB recipes being included in the Padova isochrones used by Portinari et al. (similar to our "old" dataset).

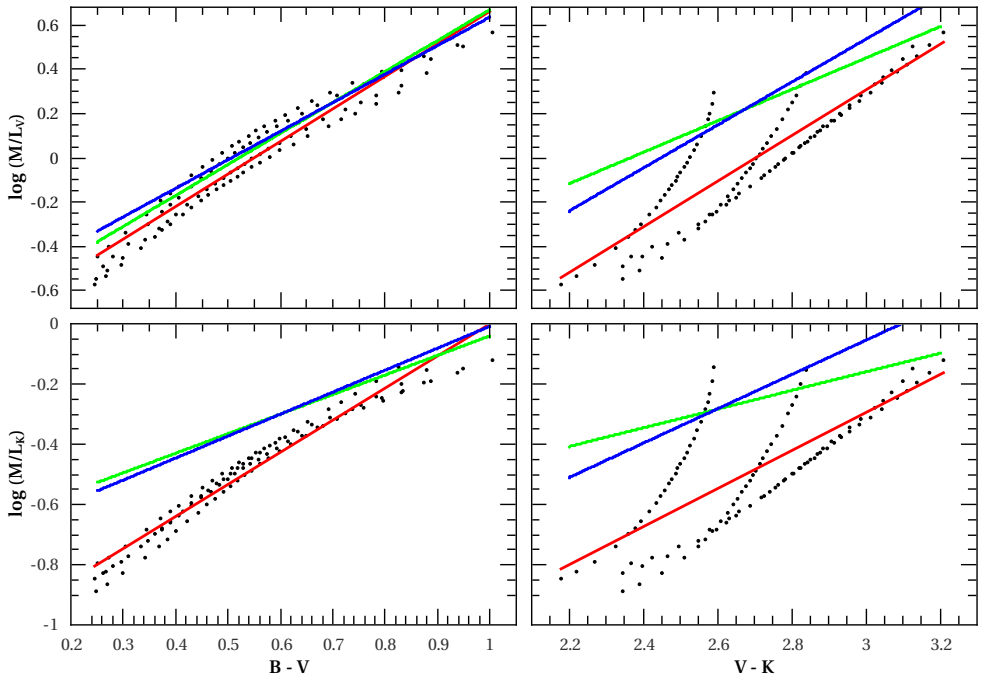

Figure 20: MLC relation fits. The dots mark our model points for metallicities $Z \geq 0.004$. The red lines are the least-squares fits to the data. Bell and de Jong (2001) and Portinari et al. (2004) relations are drawn with green and blue lines respectively.

In Figure 20 one can find sample plots of the MLC relation fits. The dots mark our model points for the four highest metallicities used for the fits. The red lines represent our MLC relations as listed in Table 4. The green lines represent the BdJ relations and the blue lines mark the Portinari relations. Inspecting the upper left panel we can see that in the optical-optical case, the three relations are very similar to each other, as already noted above. However, in the combinations involving near-IR wavelengths (K band in this case), we can see some differences in the relations. In the bottom left panel our relation differs from the other two in the blue end of the relation. The blue end consists of model points with most recent star formation episodes. Here the massive AGB stars dominate the near-IR luminosity resulting in a distinct drop in K band mass-to-light in comparison to the BdJ and Portinari relations. In the red end of $B-V$ (oldest average stellar ages), all the relations give similar M/L values. The right hand side panels show the relations in $V-K$. The age-metallicity degeneracy is quite weak in general with the exception of $Z = 0.019$ and 0.03 cases being degenerate. In $V-K$ our

relations result in lower M/L both in V and K band than the other relations. Compared to the Portinari relations, our relations are offset to lower M/L values, whereas BdJ relations differ also in the slope.

As expected, when optical colors are involved, our MLC relations are in good agreement with the results presented in the literature. As noted on several occasions in this work, the impact of the AGB phase is quite prominent in the near-infrared. With combinations involving near-IR, our relations have proven to differ by 0.2–0.3 dex in M/L from the results in the literature.

3.5 2MASS and SDSS

3.5.1 MLC relations

In Figure 21 we present the stellar M/L ratios at 2MASS H band plotted against color. Looking at the top left panel, we find the M/L ratio against the 2MASS $J-Ks$ color. It is clear that the relation is not showing an age-metallicity degeneracy, the color is clearly dependent on the metallicity to some extent, while the inter-metallicity spread in color can also be considerable, as seen in the lowest metallicity ($Z = 0.0001$) case. The same holds true for the $V-Ks$ color seen in the top right panel. In this case the two largest metallicities almost coincide, but there is still a considerable spread with metallicity in general. Naturally, fitting linear MLC relations does not make sense in these cases due to lack of sufficient degeneracy in metallicity.

One can however use the optical Johnson bands to define the colors and use them in conjunction with the 2MASS M/L ratios. In the lower panels of Figure 21 we find the H band M/L with $B-V$ (lower left panel) and $V-I$ (lower right panel) colors. We note, that the age-metallicity degeneracy is strong enough to provide reasonable MLC relations. The situation is comparable to using Johnson K band against optical colors. Again, neglecting the three lowest metallicities for the reasons mentioned earlier, the relations get tighter and produce more robust fits.

The SDSS filters are mainly in the optical region and so we expect to see a high degree of age-metallicity degeneracy as we did in the case of optical Johnson-Cousins bands. In Figure 22 we have plotted trends in the the SDSS g band M/L with color. The thick dashed lines found in all panels but one represent the MLC relations according to Bell et al. (2003). In

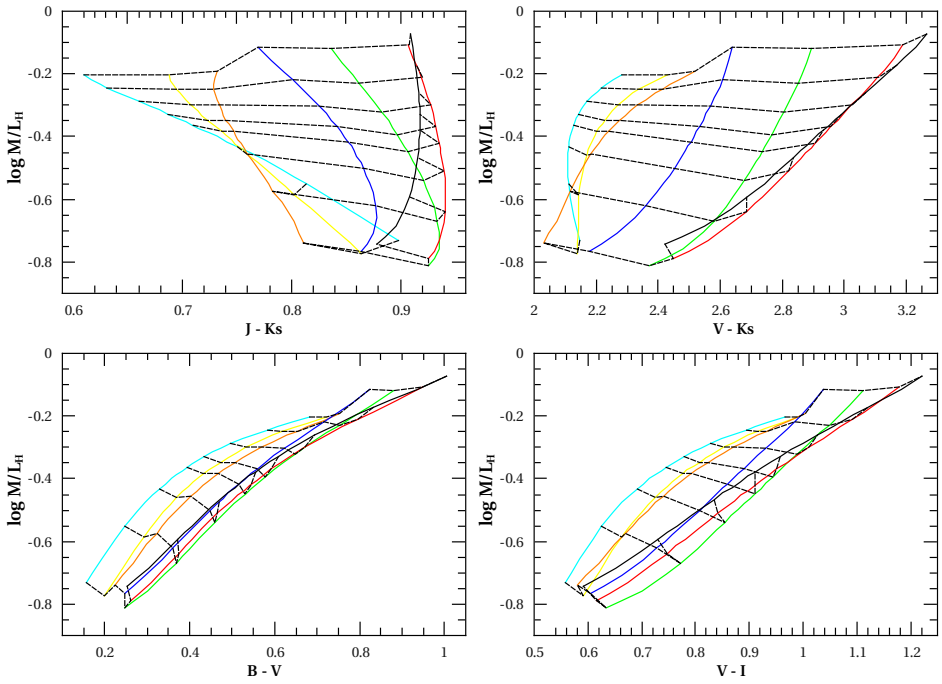

Figure 21: Trends in exponential SFH model stellar 2MASS H band M/L ratios with color. The colored solid lines connect models with the same metallicity and the dashed lines connect models with the same b parameter. The dashed lines are drawn for following subset of b values (from top to bottom): 0.01, 0.15, 0.40, 0.70, 1.00, 1.75, 3.67, 10.00.

three cases out of four, the relations are quite tight. The exception is the $i - z$ color which displays some spread in color as a function of metallicity, making it quite unsuitable for the MLC fits. The AGB phase is expected to have little effect on the SDSS bands, save for the z band, which is far enough to the red to be somewhat affected by the giant AGB stars present in the population.

3.5.2 MLC relation fits

We have constructed the fits in the same manner as described in Section 3.4.2, again including only the four highest metallicities. The resulting coefficients are presented in Table 5 for the 2MASS bands and Table 6 for the SDSS bands. Looking at the coefficients in Table 5, we can see that the slope of the relation with any given color is very similar for all the three 2MASS

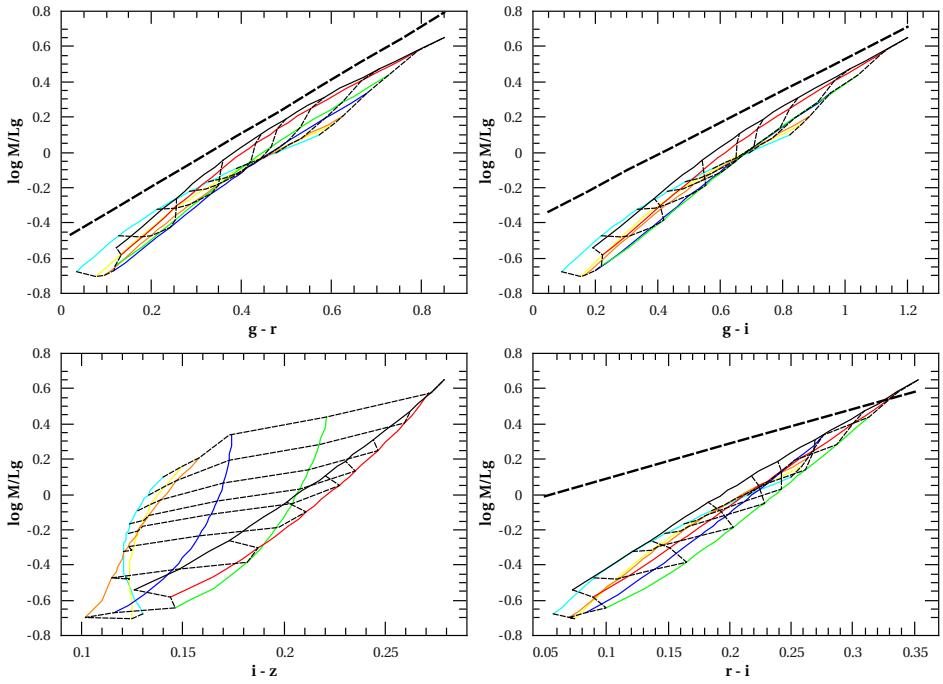

Figure 22: Trends in exponential SFH model stellar SDSS g band M/L ratios with color. Line styles as in Figure 21, thick dashed lines represent the MLC relations by Bell et al. (2003).

bands. There is a smooth decrease in the zero point of the relation with increasing wavelength. Naturally, the 2MASS relations are also very similar to the relations in Johnson-Cousins JHK bands (see Table 4 for comparison).

Bell et al. (2003) (henceforth "Bell03") presented fits for the MLC relations at SDSS bands. They applied their "least-squares fits to many passbands" methodology to derive semi-empirical MLC relations based on a large number of observed galaxies and basic evolution models. Their relations differ from our results presented in Table 6 with a varying degree. In terms of color the difference is smallest in $g-r$ and highest in $r-i$ with our fits resulting in steeper slopes. The agreement also gets worse with longer wavelengths used in M/L. Some sample relations have been plotted in Figure 22 (thick dashed lines). In $g-r$ color, the relations match very well, differing only by a slight offset in M/L. In $g-i$, in addition to the offset, the blue end of our relation bends slightly producing somewhat lower mass-to-light values and resulting in a steeper slope compared to Bell03. These differences are reasonable and can be

Color	s_J	z_J	s_H	z_H	s_{Ks}	z_{Ks}
$B-V$	1.03	-0.84	1.02	-0.99	1.05	-1.07
$B-R$	0.70	-0.95	0.70	-1.11	0.72	-1.19
$V-I$	1.27	-1.40	1.25	-1.54	1.28	-1.63
$V-K_s$	0.57	-1.85	0.54	-1.92	0.55	-2.00

Table 5: Coefficients for the linear fits to the MLC relations at 2MASS bands and for Kroupa98 IMF. Colors are in Johnson-Cousins bands and 2MASS Ks. The slope and zero points are marked with s and z respectively.

Color	s_g	z_g	s_r	z_r	s_i	z_i	s_z	z_z
$g-r$	1.77	-0.78	1.37	-0.60	1.23	-0.58	1.16	-0.62
$g-i$	1.30	-0.85	1.00	-0.65	0.90	-0.62	0.85	-0.66
$r-i$	4.71	-1.03	3.65	-0.78	3.25	-0.74	3.06	-0.77
$g-z$	1.15	-0.99	0.90	-0.76	0.80	-0.72	0.75	-0.75

Table 6: Coefficients for the linear fits to the MLC relations at SDSS bands and for Kroupa98 IMF. The slope and zero points are marked with s and z respectively.

explained by the differences in the methods used to construct the MLC relations. However, the $r-i$ color displays substantial differences between the two relations. Partly this is due to a very narrow color range that leaves the relations prone to uncertainties. Additionally, there might be some inconsistency in the Bell03 relations involving $r-i$. Using color transformation equations by Lupton (2005) and the information derived from Figure 6 of Bell03, we get a substantially steeper relation for M/L_g versus $r-i$ than the one proposed by Bell03. In any case, the use of $r-i$ color in determining stellar M/L ratios is discouraged due to the narrow baseline in color.

4 Attenuation by interstellar dust

We have already seen in Section 2.3 that the circumstellar dust of AGB stars has little effect on the integrated magnitudes of a stellar population. We concluded that this is due to a selection effect: dust is mainly present in giant PMS stars that contribute most to the total luminosity of the population in the longer wavelengths that are only mildly affected by dust reprocessing. Dust however, is also present in the interstellar medium. The interstellar dust has a dual effect, it both reddens and dims the stellar population. Considering dust effects on the MLC correlations, Bell and de Jong (2001) argue that to first order, these effects cancel out to within 0.1–0.2 dex, leaving a dust-reddened galaxy on the same color-stellar M/L ratio correlation, at least in optical MLCs. That is, a certain amount of dimming leading to a under prediction of stellar mass is compensated by an over prediction of stellar mass caused by the reddening in color. In this section we shall implement an attenuation model constructed to model reddening and extinction effects on spiral galaxies and inspect the impact it has on our simple spiral galaxy models.

4.1 Attenuation model

In describing the attenuation caused by interstellar dust we use a model by Tuffs et al. (2004). They present a method for calculating the attenuation of stellar light from spiral galaxies. The dust model used corresponds to the graphite/silicate mix of Laor and Draine (1993) and to the $a^{-3.5}$ grain size distribution of Mathis et al. (1977). The dust model is consistent with the Milky Way extinction curve.

Geometrically, the model can be divided in two components: a diffuse component and a clumpy component. The diffuse component can be related to old and young stellar populations. The old stellar population consists of bulge and disk components, while the young stellar population resides in a thin disk located inside the thicker disk component. The clumpy component is associated with the star-forming regions located in the thin disk. The bulge component is assumed to be dust-free, while for both disk components the dust distribution is modeled with an exponential disk. Radiation transfer calculations were performed separately for the three diffuse components (the bulge, disk and thin disk) to obtain the attenuation in the diffuse component and analytical means were used to obtain the attenuation for the clumpy

component. The curves of attenuation versus inclination for the diffuse components were fitted with polynomial functions and the fitting coefficients tabulated.

Tuffs et al. provide a general formula that can be used to calculate the composite attenuation at wavelength λ:

$$\Delta m_\lambda = 2.5 \log \left(r_\lambda^{\text{disk}} 10^{0.4 \Delta m_\lambda^{\text{disk}}} + \frac{1 - r_\lambda^{\text{disk}} - r_\lambda^{\text{bulge}}}{1 - F f_\lambda} 10^{0.4 \Delta m_\lambda^{\text{tdisk}}} + r_\lambda^{\text{bulge}} 10^{0.4 \Delta m_\lambda^{\text{bulge}}} \right), \tag{6}$$

where r_λ are the ratios of the apparent luminosities of disk and bulge to the total apparent luminosity:

$$r_\lambda^i = \frac{S_\lambda^i}{S_\lambda}$$

and the term $F f_\lambda$ produces the fraction of the emitted UV flux density at wavelength λ which is locally absorbed in the clumpy star-forming regions. The superscripts "disk", "bulge" and "tdisk" refer to the quantities describing the disk, bulge and thin disk respectively. The Δm_λ^i are the attenuation values in magnitudes that can be calculated using a polynomial equation:

$$\Delta m = \begin{cases} \sum\limits_{j=0,n} a_j (1 - \cos i)^j & , \ 1 - \cos i \leq 0.90 \\ b_0 & , \ 1 - \cos i = 0.95 \\ b_1 & , \ 1 - \cos i = 1.00 \, , \end{cases} \tag{7}$$

where i is the inclination of the disk and $n = 5$ for the disk and thin disk and $n = 4$ for the bulge. Values for the coefficients a_j and constants b_0 and b_1 are tabulated for a range of optical depth parameters τ_B^f and different photometric bands in Tables 4–6 of the Tuffs et al. paper. Equation 6 can be simplified if it is written separately for the UV and optical/near-IR ranges. We can approximate that the thin disk emits only in the UV range and the disk and bulge only in the optical or near-IR range. This approximation has been validated by a detailed analysis on NGC 891 (Popescu et al., 2000). Neglecting the UV term, we now have:

$$\Delta m_\lambda = 2.5 \log \left(r_\lambda^{\text{disk}} 10^{0.4 \Delta m_\lambda^{\text{disk}}} + r_\lambda^{\text{bulge}} 10^{0.4 \Delta m_\lambda^{\text{bulge}}} \right). \tag{8}$$

Free parameters

We rely on Equation 8 for calculating the attenuation effects on our spiral galaxy model. The equation has three free parameters: τ_B^f, the face-on optical depth in the B band, the inclination

i and the bulge-to-total luminosity ratio $r_\lambda^{\mathrm{bulge}}$. We will present our results with a full range of inclinations from face-on to edge-on cases with a five degree spacing. As to the bulge-to-total luminosity ratio, we will use a set of bulge-to-total mass ratios and compute the corresponding luminosity ratios resulting from these mass ratios. We will use a fixed value for the optical depth parameter: $\tau_B^f = 4.0$. This choice of parameter value is consistent with the empirical value for the mean opacity of spiral disks $\tau_B^f = 3.8 \pm 0.7$ by Driver et al. (2007) based on a sample of 10095 galaxies with bulge-disk decompositions.

4.2 Results

4.2.1 Attenuated spiral galaxy model

Our simple spiral galaxy model is composed of a 10 Gyr old SSP representing the bulge and a 10 Gyr old disk with an exponential SFH. The range of b parameters is limited to $b \leq 2.01$, covering the whole range of spiral galaxy morphologies ($b \lesssim 1$, see Section 3.2) and extending to some cases of more recent star formation. Five bulge-to-total mass ratios were chosen: 0, 0.2, 0.33, 0.5 and 0.8. The total mass of the system is set to 1 $\mathrm{M}_\odot$. For simplicity, attenuation effects were calculated for a single solar metallicity $Z = 0.019$.

Figure 23 shows the effects of interstellar dust in B band M/L vs. $B-V$ and $V-I$ colors. The solid lines represent unattenuated (dust-free) spiral galaxy models with varying b parameter values. The dots mark the attenuated model points: for each b parameter value, a full range of inclinations with a five degree spacing is presented. Different bulge-to-total mass ratios are drawn with different colors. The dashed lines are our fits to the attenuated model points. These fits will be discussed in the next section. We can clearly see that the attenuated models are somewhat redder than the dust-free ones, as expected. The reddening effect gets greater towards higher bulge-to-total (B/T) values at low b and is somewhat stronger in $V-I$ than in $B-V$.

The interstellar dust also causes extinction of the light emitted by the system, leading to a higher mass-to-light ratio. The magnitude of the increase depends on the B/T ratio and inclination. The face-on M/L value (the lowest points of each color) gets gradually higher with increasing B/T ratio. This is partly due to an increase in the average stellar age and partly due to more significant extinction of the system as bulge mass contribution raises. The counter-

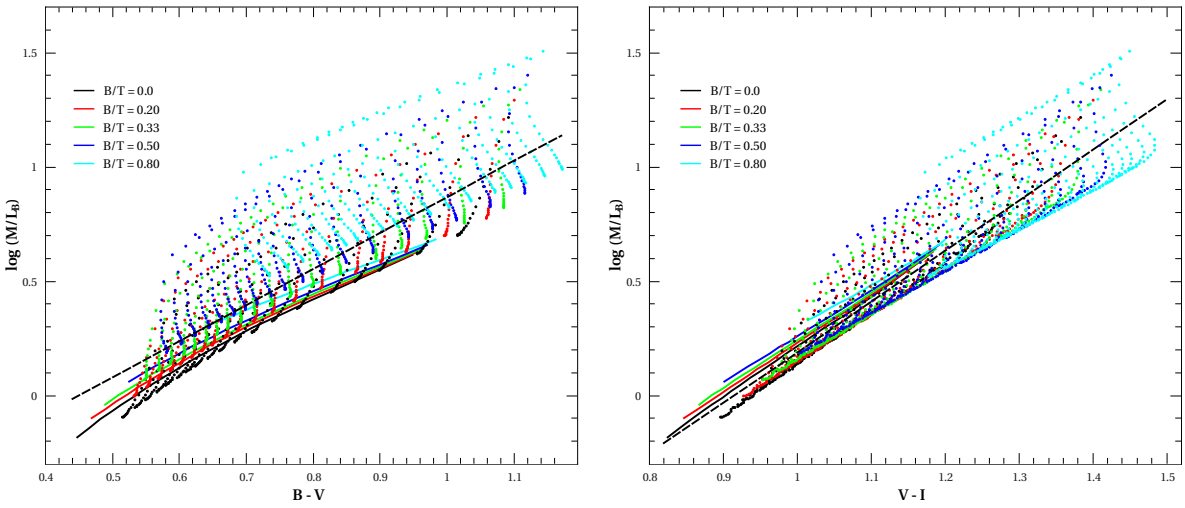

Figure 23: Attenuation due to interstellar dust in our spiral galaxy model. Logarithm of B band mass-to-light vs. $B-V$ (left panel) and $V-I$ (right panel). Solid lines connect the unattenuated (dust free) models with $b \leq 2.01$. Models with different bulge-to-total mass ratios are distinguished by colors. Dots mark the attenuated model points. The b parameter value increases from right to left and inclination from top to bottom. The dashed lines indicate our fits to the attenuated models (see Section 4.2.2 for details).

intuitive idea of a spiral galaxy suffering from a greater amount of extinction from having a larger bulge and hence a smaller amount of dust in the galaxy is a result from the bulge being the most attenuated component in the galaxy (see Driver et al. 2007). The light originating from parts of the bulge that are obscured by the disk is attenuated more efficiently than the light originating from the disk because all of it has to pass through the whole surrounding disk (assuming a non-zero inclination), whereas the light from the disk has to pass through same amount or less dust, depending on its origin.

The spread in M/L as a function of inclination is constant for a given band and independent of the B/T ratio. In $B-V$ the changes in inclination mainly result in changes in the M/L ratio, with little effect on the color. In $V-I$, varying inclination at low values results in a small change both in the color and M/L, while at higher inclinations, there is a sudden turn in the trend and the M/L ratio rises rapidly. Moving to colors involving even longer wavelengths, the nature of the inclination dependence changes. As seen in Figure 24, both $V-J$ and $V-K$

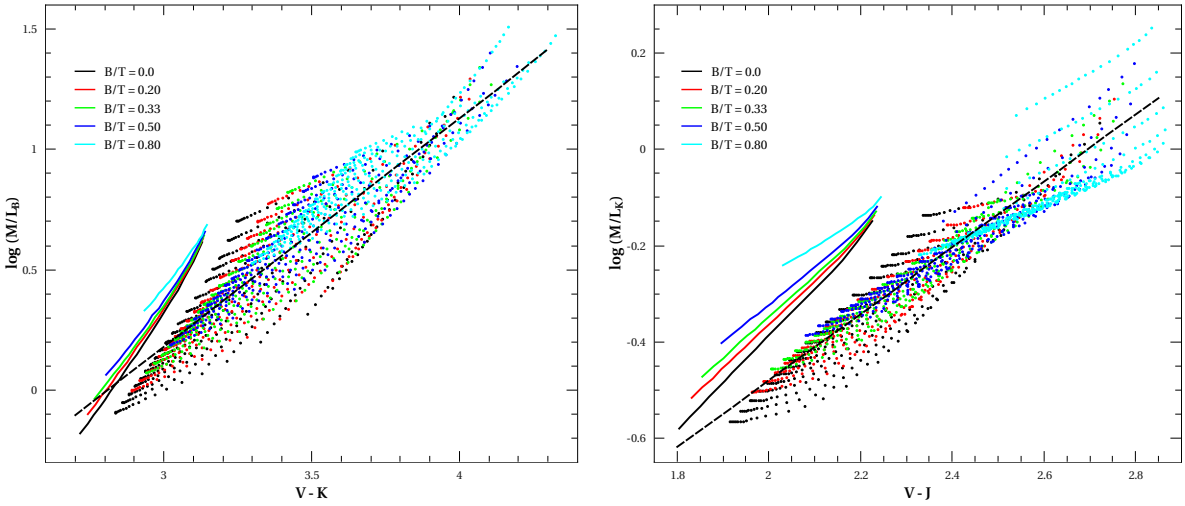

Figure 24: *Left panel:* Logarithm of B band M/L vs. $V - K$ color. *Right panel:* Logarithm of K band M/L vs. $V - J$ color. Line styles as in Figure 23.

colors are strongly dependent on the galaxy inclination. Thus, in the optical regime, there is only a weak relation between inclination and color of the system, while towards near-IR, we can see an obvious trend in color with higher inclinations producing redder colors.

The right panel of Figure 24 confirms the general assumption that the mass-to-light ratio in the near-IR bands is not as prone to extinction as the visual bands and we also see that the spread in K band M/L as a function of inclination is much narrower than in the B band.

4.2.2 Attenuation effects on MLC relations

The question is then: How does the attenuation due to interstellar dust affect the MLC relations? According to Bell and de Jong (2001), the reddening caused by the dust is counterbalanced with a suitable amount of extinction, leaving the relation virtually untouched. In Table 7 we have tabulated the MLC relation coefficients for our galaxy model with $b \leq 2.01$, both attenuated and unattenuated. In Figures 23 and 24 we have plotted the fits for attenuated models with dashed lines. For these fits, we have neglected the $B/T = 0.8$ case as this ratio is considered to be on the limit of being an elliptical rather than a spiral galaxy (Allen et al., 2006). The observed distribution of spiral galaxy B/T luminosity ratios is found to be quite flat (Driver et al., 2007). This justifies the fitting of the attenuated models with an equal weight

					Unattenuated					
color	s_B	z_B	s_V	z_V	s_I	z_I	s_J	z_J	s_K	z_K
$B-V$	1.49	−0.76	1.09	−0.49	0.82	−0.42	0.77	−0.63	0.77	−0.85
$V-I$	2.17	−1.93	1.59	−1.36	1.19	−1.07	1.12	−1.24	1.13	−1.47
$V-J$	1.82	−3.45	1.34	−2.48	1.00	−1.91	0.94	−2.02	0.95	−2.26
$V-K$	1.87	−5.24	1.37	−3.79	1.03	−2.89	0.96	−2.94	0.97	−3.19
					Attenuated					
$B-V$	1.58	−0.71	1.18	−0.44	0.88	−0.38	0.78	−0.61	0.75	−0.85
$V-I$	2.21	−2.02	1.71	−1.49	1.31	−1.21	1.14	−1.31	1.04	−1.46
$V-J$	1.52	−3.01	1.24	−2.41	1.00	−2.02	0.84	−1.95	0.69	−1.86
$V-K$	0.95	−2.67	0.81	−2.25	0.68	−1.99	0.56	−1.88	0.41	−1.65

Table 7: MLC fits to our simple galaxy model with $b \leq 2.01$ and single metallicity $Z = 0.019$. The coefficients s_i present the slopes of the MLC relation at various bands. Both attenuated and unattenuated cases are displayed.

on each point.

We note that in $B-V$ the attenuated models display slightly higher optical MLC relation slope values accompanied with a small shift towards higher M/L compared to the unattenuated models (see the left panel of Figure 23). The difference in slope is not very significant, but there is approximately a 0.1 dex offset. In the near-IR bands, the attenuation hardly changes the relations at all. When inspecting the left panel of Figure 23 one can see that even though the spread in M/L with inclination is large, most of the points with inclinations $i \lesssim 60$ degrees occupy a rather narrow range close to the unattenuated values, leaving little weight on the high inclination values. In $V-I$ the difference between the MLC relations is somewhat smaller than in $B-V$. As discussed earlier, here the inclination also affects the color of the system and not just the M/L ratio. As seen in the right panel of Figure 23, the trend in inclination follows a path rather parallel to the unattenuated model for a substantial range of inclinations, only the highest inclinations cause a substantial increase in M/L. In the K band, the relation is actually more gradual in the attenuated case. The K band M/L is not strongly affected by attenuation, but the $V-I$ color gets somewhat redder which results in a more gradual

relation. The most prominent changes in MLC relations can be seen in $V-J$ and $V-K$ colors over the whole range of bands (see Figure 24). As we have already noted, in these cases the attenuation strongly affects the colors of the system. This results in significant differences between the attenuated and unattenuated MLC relations. When combining optical and near-IR wavelengths in colors, the reddening effect dominates. This makes the MLC relations for the attenuated models much shallower than for the unattenuated models.

We conclude that when using optical colors (combinations involving $UBVRI$ bands or similar), the interstellar dust does not severely affect the MLC relations, as suggested by BdJ. This applies to the statistical properties of spiral galaxies. However, the mass-to-light ratio of an individual galaxy of high inclination can be significantly underestimated if the dust effects are not properly taken into account. We also find that among the colors used, $V-I$ is most robust against attenuation effects. Moving towards colors involving near-IR wavelengths, the reddening effect dominates over extinction leading to a greater disagreement between the attenuated and unattenuated MLC relations.

5 Conclusions

On many occasions in this work we have witnessed the importance of proper treatment of the asymptotic giant branch phase in the stellar evolutionary population synthesis. The calculations by Maraston (1998) of the relative contribution of the AGB phase luminosity to the total bolometric luminosity of a SSP peaking around 40 percent based on the fuel consumption theorem were confirmed in our SSP calculations based on the recent AGB models. This alone is a compelling piece of evidence in favor for the importance of the AGB phase. We have also seen that omitting the AGB phase from the EPS models can lead to significant changes in the mass-to-light–color relations, especially those involving near-IR bands (Section 3.4.1).

The main purpose of this work was to implement EPS models using the updated Padova stellar isochrones with improved AGB phase modeling and provide updated MLC relations for populations with extended star formation histories. Besides that, we wanted to highlight the differences between models using the old and the new sets of Padova isochrones. The SSPs showed that while there was little difference between the different sets in the optical regime, this was not the case with near-IR bands, where the new models were consistently more luminous than the old models. We also investigated the effect of circumstellar dust on the SSPs and found that it is negligible: the impact of dust on the integrated magnitudes is far less than the difference between the old and the new sets of isochrones.

As to the MLC relations themselves, we found that in the optical regime, our relations agree quite well with previous theoretical relations presented in the literature. This was an expected result since the AGB phase does not contribute much to the integrated light of the population in the optical wavelengths. However, when near-infrared colors or luminosities were involved, our relations deviated quite significantly from previous ones. This is important to notice if one wishes implement the MLC relations in the near-IR bands. The near-IR bands are frequently used in mass estimates as these wavelengths are more robust against dust attenuation effects and recent bursts of star formation. But neglecting the proper treatment of TP-AGB phase in stellar population synthesis models can lead to significant errors in the mass estimates derived using these relations. Similarly, when implementing the interstellar dust attenuation models to our model spiral galaxy, we found that in the optical colors, the interstellar dust did not change the MLC relations very much from the unattenuated cases, thus agreeing with the conclusions presented in Bell and de Jong (2001). But using colors

involving optical-near-IR combinations, a distinct change in the MLC relations was observed. The MLC relations we derived for the dust attenuated spiral galaxies are meant to be applied statistically to a large sample of galaxies with varying inclinations. The relations are not applicable to individual galaxies due to a large spread in M/L as a function of inclination.

The Padova isochrones currently provide a satisfactory level of detail in describing the TP-AGB evolution. But the AGB evolutionary models are still far from being complete. Further improvements will be needed to solve the problems with the low-metallicity mass loss formulations that cause some extra luminosity in SSPs with ages around 10 Gyr. But EPS models are not all about the AGB phase. Even if the AGB phase could be mastered without a flaw, there are still many other factors contributing in the uncertainties of the EPS models. Such factors can be found in some stages of single or binary star evolution, interstellar dust treatment and stellar spectral libraries, among others. Refining the EPS models requires improvements in the underlying basic physics in all of these fields, meaning that the population synthesis method has yet to reach its full potential.

References

Allen, P. D., Driver, S. P., Graham, A. W., Cameron, E., Liske, J., and Propris, R. D.: 2006, *Mon. Not. R. Astron. Soc.* **371**, 2

Arimoto, N. and Yoshii, Y.: 1986, *Astron. Astrophys.* **164**, 260

Arimoto, N. and Yoshii, Y.: 1987, *Astron. Astrophys.* **173**, 23

Bakos, J., Trujillo, I., and Pohlen, M.: 2008, *Astrophys. J., Lett.* **683**, 103

Bell, E. F. and de Jong, R. S.: 2001, *Astrophys. J.* **550**, 212

Bell, E. F., McIntosh, D. H., Katz, N., and Weinberg, M. D.: 2003, *Astrophys. J., Suppl. Ser.* **149**, 289

Bressan, A., Granato, G. L., and Silva, L.: 1998, *Astron. Astrophys.* **332**, 135

Bruzual, G.: 2007, in A. Vallenari, R. Tantalo, L. Portinari, and A. Moretti (eds.), *From Stars to Galaxies: Building the Pieces to Build Up the Universe*, Vol. 374, p. 303, Publ. Astron. Soc. Pac., San Francisco

Bruzual, G. and Charlot, S.: 2003, *Mon. Not. R. Astron. Soc.* **344**, 1000

Carraro, G.: 2000, *The Evolution of the Milky Way: Stars versus Clusters*, Vol. 255, Kluwer ASSL

Chabrier, G.: 2001, *Astrophys. J.* **554**, 1274

Chiosi, C., Bertelli, G., and Bressan, A.: 1992, *Annu. Rev. Astron. Astrophys.* **30**, 235

CMD 2.2, http://stev.oapd.inaf.it/cgi-bin/cmd, referred Sep 23th 2009

Driver, S. P., Popescu, C. C., Tuffs, R. J., Liske, J., Graham, A. W., Allen, P. D., and Propris, R. D.: 2007, *Mon. Not. R. Astron. Soc.* **379**, 1022

Frogel, J. A., Mould, J., and Blanco, V. M.: 1990, *Astrophys. J.* **352**, 96

Girardi, L. and Bertelli, G.: 1998, *Mon. Not. R. Astron. Soc.* **300**, 533

Girardi, L., Bertelli, G., Bressan, A., Chiosi, C., Groenewegen, M. A. T., Marigo, P., Salasnich, B., and Weiss, A.: 2002, *Astron. Astrophys.* **391**, 195

Girardi, L., Bressan, A., Bertelli, G., and Chiosi, C.: 2000, *Astron. Astrophys. Suppl. Ser.* **141**, 371

Groenewegen, M. A. T.: 2006, *Astron. Astrophys.* **448**, 181

Iben, Jr., I.: 1991, *Astrophys. J., Suppl. Ser.* **76**, 55

Izzard, R. G., Tout, C. A., Karakas, A. I., and Pols, O. R.: 2004, *Mon. Not. R. Astron. Soc.* **350**, 407

Karakas, A. I., Lattanzio, J. C., and Pols, O. R.: 2002, *Proc. Astron. Soc. Aust.* **19**, 515

Kassin, S. A., de Jong, R. S., and Weiner, B. J.: 2006, *Astrophys. J.* **643**, 804

Kennicutt, Jr., R. C., Tamblyn, P., and Congdon, C. W.: 1994, *Astrophys. J.* **435**, 22

Kranz, T., Slyz, A., and Rix, H.-W.: 2003, *Astrophys. J.* **586**, 143

Kroupa, P.: 1998, in R. Rebolo, E. Martin, and M. Zapatero Osorio (eds.), *Brown Dwarfs and Extrasolar Planets*, Vol. 134, p. 483, Publ. Astron. Soc. Pac., San Francisco

Kroupa, P.: 2001, *Mon. Not. R. Astron. Soc.* **322**, 231

Laor, A. and Draine, B. T.: 1993, *Astrophys. J.* **402**, 441

Lupton, R., *Transformations between SDSS magnitudes and UBVRcIc*, http://www.sdss.org/dr6/algorithms/sdssUBVRITransform.html, referred May 29th 2010

Maraston, C.: 1998, *Mon. Not. R. Astron. Soc.* **300**, 872

Marigo, P. and Girardi, L.: 2007, *Astron. Astrophys.* **469**, 239

Marigo, P., Girardi, L., Bressan, A., Groenewegen, M. A. T., Silva, L., and Granato, G. L.: 2008, *Astron. Astrophys.* **482**, 883

Mathis, J. S., Rumpl, W., and Nordsieck, K. H.: 1977, *Astrophys. J.* **217**, 425

Paczynski, B.: 1975, *Astrophys. J.* **202**, 55

Popescu, C. C., Misiriotis, A., Kylafis, N. D., Tuffs, R. J., and Fischera, J.: 2000, *Astron. Astrophys.* **362**, 138

Portinari, L., Chiosi, C., and Bressan, A.: 1998, *Astron. Astrophys.* **334**, 505

Portinari, L., Sommer-Larsen, J., and Tantalo, R.: 2004, *Mon. Not. R. Astron. Soc.* **347**, 691

Renzini, A. and Buzzoni, A.: 1986, in C. Chiosi and A. Renzini (eds.), *Spectral Evolution of Galaxies*, Reidel, Dordrecht

Renzini, A. and Voli, M.: 1981, *Astron. Astrophys.* **94**, 175

Salpeter, E. E.: 1955, *Astrophys. J.* **121**, 161

Scalo, J. M.: 1986, *Fundam. Cosmic Phys.* **11**, 1

Tinsley, B. M.: 1980, *Fundam. Cosmic Phys.* **5**, 287

Tuffs, R. J., Popescu, C. C., Völk, H., Kylafis, N. D., and Dopita, M.: 2004, *Astron. Astrophys.* **419**, 821

Ventura, P., D'Antona, F., and Mazzitelli, I.: 2002, *Astron. Astrophys.* **393**, 215